Reviews in Mineralogy & Geochemistry
Vol. 89 pp. 691-727, 2023
Copyright © Mineralogical Society of America

Tectonics of the Moon

**Amanda L. Nahm[1], Thomas R. Watters[2], Catherine L. Johnson[3,4],
Maria E. Banks[2,4,5], Carolyn H. van der Bogert[6], Renee C. Weber[7],
Jeffrey C. Andrews-Hanna[8]**

*[1]NASA Headquarters, 300 E Street SW, Washington,
District of Columbia 20024-3210 U.S.A.*

*amanda.l.nahm@nasa.gov**

*[2]Center for Earth and Planetary Studies, National Air and Space Museum,
Smithsonian Institution, Washington, District of Columbia 20560 U.S.A.*

*watterst@si.edu**

*[3]Department of Earth, Ocean, and Atmospheric Sciences,
University of British Columbia, Vancouver, British Columbia, Canada*

*[4]Planetary Science Institute, 1700 E Fort Lowell Rd STE 106,
Tucson, Arizona 87519, U.S.A.*

cjohnson@eoas.ubc.ca

[5]NASA Goddard Space Flight Center, Greenbelt, Maryland, U.S.A.

maria.e.banks@nasa.gov

*[6]Institut für Planetologie, Westfälische Wilhelm-Universität Münster
Wilhelm-Klemm-Str. 10, 48149 Münster, Germany*

vanderbogert@uni-muenster.de

*[7]NASA Marshall Space Flight Center, Huntsville,
Alabama 35812, U.S.A.*

renee.c.weber@nasa.gov

*[8]Lunar and Planetary Laboratory, University of Arizona,
Tucson, Arizona 85721, U.S.A.*

jcahanna@gmail.com

* = *corresponding authors*

1. SUMMARY

In less than a decade, the long-held view that the tectonics of the Moon were largely just a consequence of the evolution of the near side mare basins has been changed dramatically. The discovery of a vast population of small-scale lobate thrust fault scarps in images returned by the Lunar Reconnaissance Orbiter Camera (LROC) has provided evidence that the Moon

1529-6466/23/0089-0016$05.00 (print)
1943-2666/23/0089-0016$05.00 (online)
http://dx.doi.org/10.2138/rmg.2023.89.16

experienced global-scale tectonics. Efforts to date these small fault scarps indicate a young age, actively forming within the last 50 to 100 Ma. High-resolution images and topographic data obtained by the Lunar Orbiter Laser Altimeter (LOLA) and LROC stereo imaging have enabled a new generation of global tectonic maps of wrinkle ridges and graben, allowing morphologic and dimensional analysis of these landforms in unprecedented detail. An unparalleled new view of the Moon's crustal structure provided by the Gravity Recovery and Interior Laboratory (GRAIL) mission, along with the new tectonic data sets, hint at a more complex evolution of near side mare than previously thought, and perhaps present some challenges to classic mascon tectonic models. For example, a large, regional-scale rift system bordering Oceanus Procellarum and Mare Frigoris discovered in GRAIL gravity gradient maps may have influenced mare tectonics. GRAIL has also revealed evidence of widely-distributed ancient buried rifts, graben, and dike intrusions that formed early in the Moon's thermal evolution when the dominant stress state was extensional. The young thrust faults and young small-scale graben detected in LROC images provide a window into the recent stress state of the Moon and offer insights into the origin of current lunar near-surface stresses. The global pattern of lobate fault scarps is consistent with stresses from global contraction in combination with tidal stresses from recent true polar wander, orbital recession, and Earth-raised diurnal tides. The young age of the fault scarps raises the possibility that coseismic slip events on the developing faults were recorded by the Apollo Seismic Network. Some relocated epicenters of recorded shallow moonquakes are in close proximity (<30 km) to mapped fault scarps. The emerging new view of the Moon as more tectonically dynamic in its ancient past and as a potentially still active body may give fresh insight into the formation and tectonic evolution of small, one-plate rocky bodies.

2. INTRODUCTION AND MOTIVATION

On the Moon, tectonic landforms occur globally, but with distinct types concentrated on the near side, associated spatially with lunar maria. Previously, three main types of tectonic structures on the Moon were identified: basin-localized compressional wrinkle ridges and extensional graben and the more broadly-distributed lobate scarps. Tectonic landforms are a direct expression of the state of stress in the Moon's near-surface crustal materials at the time of deformation. Thus, the spatial distribution, morphometry (lengths, widths, and reliefs), as well as absolute and relative ages of such structures, provide critical constraints on the temporal and spatial evolution of stress in the lunar lithosphere.

Lunar wrinkle ridges are one of the earliest recognized extraterrestrial tectonic landforms, seen first in Earth-based telescopes. G. K. Gilbert described the ridges as anticlinal forms over one hundred years ago (Gilbert 1893). Their exclusive occurrence in mare basalts, however, spawned an early debate that extended into the Apollo era over whether wrinkle ridges were volcanic or tectonic in origin. Some concluded the association with maria as evidence that wrinkle ridges are volcanic ridges related to either the emplacement, intrusion, or extrusion of mare lava (Fielder 1961; Quaide 1965; Whitaker 1966; Tija 1970; Hartmann and Wood 1971; Colton et al. 1972; Strom 1972; Hodges 1973; Scott 1973; Young et al. 1973). Like Gilbert (1893), others concluded that wrinkle ridges are purely tectonic landforms (Baldwin 1963, 1965; Bryan 1973; Hodges 1973; Howard and Muehlberger 1973; Schaber 1973; Muehlberger 1974; Maxwell et al. 1975; Lucchitta 1976; 1977; Maxwell and Phillips 1978; Sharpton and Head 1981, 1982, 1988). Images returned by robotic missions to Mercury, Venus, and Mars show that wrinkle ridges are found in volcanic plains on all the terrestrial planets (Watters and Schultz 2010).

Structures previously termed linear and arcuate rilles are long, narrow troughs interpreted to be graben formed by extension, deforming both mare basalts at basin margins and the adjacent highlands. They are thus primarily located on the lunar near side. Their highly symmetric cross-sectional geometry and characteristic flat floors with steeply inward-dipping walls led to the nearly unanimous interpretation that they are graben formed by crustal extension (Baldwin 1963; Quaide 1965; McGill 1971; Lucchitta and Watkins 1978). The basin-localized nature of both wrinkle ridges and graben was interpreted in terms of lithospheric loading by volcanism that produced the mare basalts (see review in Watters and Johnson 2010), constraining stresses to the mare-filled basins after the major episodes of mare magmatism. Basin-localized extension was inferred to have ceased ~3.6 Ga ago (Lucchitta and Watkins 1978), with crustal shortening continuing to ~1.2 Ga (Hiesinger et al. 2003).

Lobate scarps on the Moon are relatively small tectonic landforms that were first detected only in high-resolution Apollo Panoramic Camera and Lunar Orbiter (LO) photographs (Mattingly et al. 1972; Schultz 1976a; Masursky et al. 1978). Because of the relatively small size of the scarps and the limited coverage of the Panoramic Camera and LO photographs (i.e., limited to a portion of the lunar equatorial zone), only relatively few lobate scarps had been identified and their global number and spatial distribution was previously unknown (Binder 1982; Binder and Gunga 1985; Watters and Johnson 2010). These structures were generally inferred to be ~1 Ga and younger, and, by analogy with the similar but much longer and larger relief structures on Mercury (Strom et al. 1975; Watters et al. 1998), were inferred to be an expression of global contraction resulting from interior cooling (Strom et al. 1975; Melosh and McKinnon 1988; Watters et al. 1998; Hauck et al. 2004).

Over the past decade, the Moon has been explored extensively with new high-resolution imaging, topography and gravity data sets (Section 3 and Gaddis et al. 2023, this volume). These have enabled tectonic structures to be mapped in unprecedented detail. Key aspects of tectonic features relevant to understanding the evolution of stress in the lunar crust are their global distribution, relief and length, orientation, and ages. Significant progress has been made in all of these aspects with new data sets for lobate scarps, wrinkle ridges, and graben now available (Sections 4.1, 4.2, 4.3). In addition, new classes of features, not identifiable in previous data sets, have been discovered. Specifically, high-resolution images have provided evidence for very young, small-scale graben (Section 4.4) and gravity data have provided evidence for ancient, buried extensional structures with no surface expression (Section 4.5). In this chapter, we summarize progress in the characterization of lunar tectonic landforms over the past decade, including improved constraints on their ages (Sections 4 and 5). We discuss what these new data sets reveal about the Moon's evolution and recent activity (Section 6). In particular, we show that the new data sets have been able to address some previous outstanding issues (Watters and Johnson 2010), namely (i) the global distribution and ages of lobate scarps, (ii) the nature of tectonism in and around Oceanus Procellarum and constraints on the origin of Oceanus Procellarum, (iii) knowledge of subsurface structures, and (iv) understanding of recent tectonism and any connection to present-day seismicity. The discoveries reviewed here are thus intimately linked in terms of understanding to lunar interior structure (Andrews-Hanna et al. 2023, this volume). We conclude with some remarks on possible future directions for research on the tectonics of the Moon.

3. NEW GLOBAL DATASETS FOR TECTONIC STUDIES

More than 15 spacecraft have been sent to the Moon since 2006, including several impactors, landers, and orbiters. These spacecraft collected four types of data relevant to tectonic studies: 1) high resolution imagery, 2) laser altimetry, 3) gravity, and 4) radar sounding. Digital elevations models (DEMs) have been derived from laser altimetry, stereo imaging, and combination of the two. In particular, image data were collected by the CCD Stereo Camera onboard the Chinese orbiter Chang'E-1 (launched 2007), the Terrain Camera (TC) onboard the Japanese SELenological and ENgineering Explorer (SELENE) (Kaguya) orbiter (launched 2007), and the Lunar Reconnaissance Orbiter Camera (LROC) onboard the

Lunar Reconnaissance Orbiter (LRO, launched 2009). Laser altimetry data were collected by the Chang'E-1, SELENE, and LRO missions, as well as the Indian Chandrayaan-1 mission (launched 2008). For detailed descriptions of the missions, their instruments, and where to find their data, please see Gaddis et al. (2023, this volume).

4. TECTONIC STRUCTURES

4.1. Lobate scarps

4.1.1. Morphology and morphometry. Lobate scarps are morphologically simple landforms that express contraction of crustal materials (Howard and Muehlberger 1973; Lucchitta 1976; Schultz 1976a; Binder 1982; Binder and Gunga 1985; Watters and Johnson 2010; Watters et al. 2010). In plan view, lobate scarps are typically linear to arcuate landforms. In cross section, they are generally asymmetric, with steeply sloping scarp faces (~ 5°–29°) and more gently sloping back-scarp terrain (Fig. 1) (Watters and Johnson 2010; Watters et al. 2010; Banks et al. 2012). LROC images and stereo-derived digital terrain models (DTMs) (Robinson et al. 2010) enable detailed morphometric analysis of the lobate thrust fault scarps (Banks et al. 2012; Watters et al. 2015a). Lobate scarps average tens of meters of relief, reaching a maximum of ~ 150 m and have lengths of up to tens of kilometers (Binder and Gunga 1985; Banks et al. 2012). The lunar scarps are about an order of magnitude smaller in scale than the largest lobate scarps on Mercury and Mars and thrust fault structures on Earth, which have reliefs of > 1 km and lengths of hundreds of kilometers (Watters 2003; Watters et al. 2009; Watters and Nimmo 2010), but are comparable in scale to recently-detected young thrust fault scarps on Mercury (Watters et al. 2016).

The morphology and dimension of lunar lobate scarps is directly influenced by the geometry, depth, and cumulative slip on their underlying thrust faults. Detailed topography obtained from LROC Narrow Angle Camera (NAC) stereo-derived DTMs has been used to constrain elastic dislocation modeling of lunar scarps (Williams et al. 2013). Model results for six lunar lobate scarps show that the morphology and dimensions are very well approximated by deformation from planar thrust faults with dip angles of 35° to 40° and maximum depths of faulting from a few hundred meters to about 1 km (Williams et al. 2013). Employing a method that assumes arcuate segments of some lunar scarps are controlled by thrust faults with conical geometries (Binder 1982), dip angles ranging from 4° to 46° (mean 23°) were obtained for

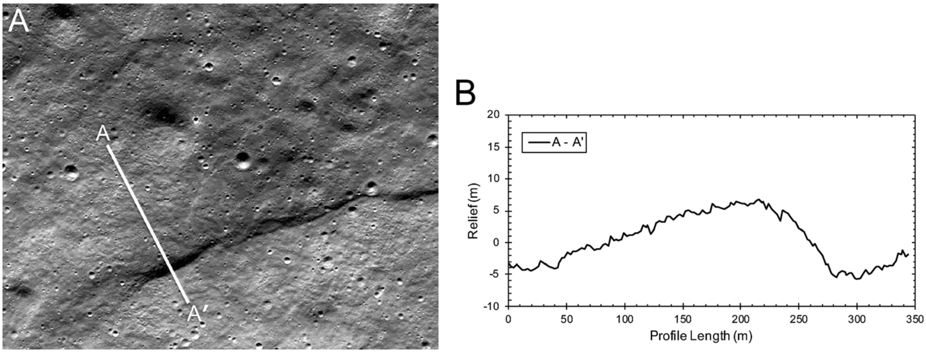

Figure 1. Lobate scarp Simpelius-1 and topographic profile. **A)** The lobate scarp is located on the located on the wall of Simpelius crater (~73.6°S, 13.0°E) (Banks et al. 2012). The **white line** indicates the location of the topographic profile shown in 1B. LROC NAC image M139804021LE. **B)** Topographic profile across Simpelius-1 from a LROC NAC stereo-derived DTM. The detrended profile shows that the vergent side of the scarp is upslope on the crater wall. The DTM has a horizontal spatial scale of 2 m and was generated using NAC stereo images M139804021LE, M139804021RE, M139817589LE, and M139817589RE. The vertical exaggeration is ~6.

five lunar scarps (Clark et al. 2017a). A range of fault dips of 35° to 40° is comparable to those estimated for lobate scarps on asteroid 433 Eros (Watters et al. 2011) and larger scarps on Mercury and Mars (Schultz and Watters 2001; Watters et al. 2002).

4.1.2. Global distribution. In spite of their diminutive size, lobate scarps have emerged as one of the most common tectonic landforms on the Moon. The new high-resolution images and topography data from stereo imaging (summarized in Gaddis et al. 2023, this volume) have allowed identification of many previously unrecognized scarps as short in length as 100 m, and greatly improved characterization of their reliefs. Over 3,500 individual scarps have been identified and mapped to date (Fig. 2) (Watters et al. 2015a). They are observed principally in the highlands and are globally distributed, occurring at all latitudes on both the near side and far side (Watters et al. 2010, 2015a; Banks et al. 2012). Although lobate scarps are the dominant tectonic landform in the lunar highlands, some are also found in mare basalts (~3% of mapped scarps) and in highlands at the margins of mare deposits (~4% of those mapped) (Watters et al. 2015a). The thrust fault scarps commonly crosscut impact craters and are often observed on crater walls where the vergence direction is frequently oriented upslope (Mattingly et al. 1972; Schultz 1976a; Masursky et al. 1978; Banks et al. 2012; Roggon et al. 2017). The small lunar thrust faults are almost always observed in clusters consisting of multiple individual scarps with parallel/subparallel orientations that are often *en echelon*. Some clusters can extend for large distances, such as the ~250 km long north-east trending Vitello cluster south of Mare Humorum (Fig. 2). Overall, lobate scarps are oriented broadly N–S at low- to mid-latitudes and E–W at high latitudes, though some structures are oriented N–S at high latitudes (Watters et al. 2015a).

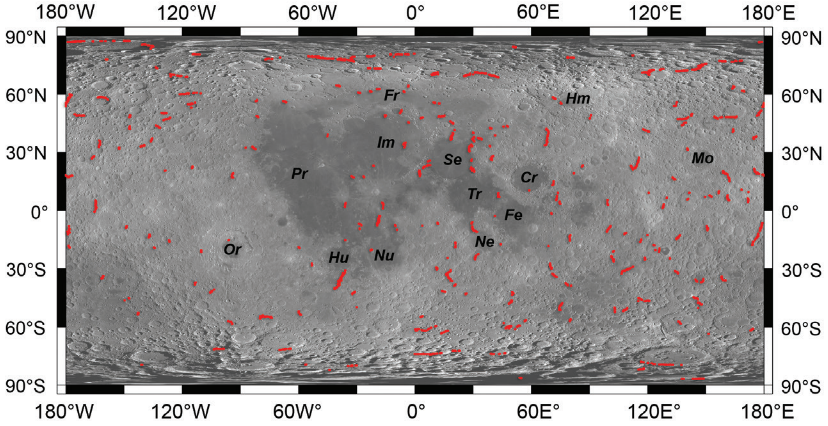

Figure 2. Global map showing more than 3,500 mapped lobate scarps. Because many are very small, they overlap at the scale of this map (from Watters et al. 2019). Basemap: LROC WAC global morphologic map, 100 m/px, in equidistant cylindrical projection. Mare Frigoris (Fr), Mare Imbrium (Im), Oceanus Procellarum (Pr), Mare Serenitatis (Se), Mare Crisium (Cr), Mare Tranquillitatis (Tr), Mare Fecunditatis (Fe), Mare Nectaris (Ne), Mare Nubium (Nu), Mare Humorum (Hu), Mare Moscoviense (Mo), Mare Orientale (Or), Mare Humboldtianum (Hm).

4.1.3. Formation mechanisms. A number of attributes provide evidence that lunar lobate scarps are the surface expression of thrust faults (Howard and Muehlberger 1973; Lucchitta 1976; Binder 1982; Binder and Gunga 1985; Watters and Johnson 2010; Watters et al. 2010, 2015a; Banks et al. 2012; Williams et al. 2013; Clark et al. 2017a; Roggon et al. 2017). In addition to their general morphology, these characteristics include scarp segment linkage, reversals in vergence of *en echelon* stepping scarps, and upslope vergence.

Thrust faults associated with lobate scarps are formed in response to contraction of near-surface crustal materials. Compressional stresses inducing contraction must exceed the local strength of the crustal material to initiate faulting. The surface expression of cumulative slip on the developing thrust fault is strongly influenced by the bulk mechanical properties of the displaced crustal materials. The lunar highlands, where the vast majority of the lobate scarps occur, are devoid of the type of layering inherent in mare basalts (Watters and Johnson 2010). At the depths which lobate scarp thrust faults are likely to extend (upper few kilometers) the highlands are thought to be mechanically homogeneous and isotropic because the ancient highlands crust has been subjected to billions of years of impact cratering resulting in a thick megaregolith. This is not to suggest that the lunar highlands are mechanically homogeneous and isotropic at depth. In fact, high-resolution gravity data from GRAIL (Zuber et al. 2013a) indicate that porosity decays exponentially with depth (Besserer et al. 2014) likely resulting in an increase in mechanical strength. The bulk density of the lunar highlands crust from GRAIL data is estimated to be 2550 kg·m^{-3} (Wieczorek et al. 2012). The bulk density is a key parameter in estimating the frictional strength of the highlands crust, and this in turn constrains the depth to which thrust faults may extend (Williams et al. 2013). The lack of strong mechanical layering of the upper few kilometers of the highlands is the likely factor controlling the relatively simple morphology of lunar lobate scarps (Watters 1988; Watters and Johnson 2010).

4.1.4. Displacement–length relationship. It is now well established from studies of terrestrial faults that the maximum displacement on a fault $D_{\max}$ scales with its planimetric length L (e.g., Walsh and Watterson 1988; Cowie and Scholz 1992a,b), and that this relationship also holds for faults on other bodies (Schultz et al. 2010a). Measurements of the maximum relief h of individual lobate scarp segments have been used to estimate the maximum displacement on associated thrust faults using the relationship $D_{\max} = h/\sin\theta$, where θ is the dip of the surface-breaking fault plane (e.g., Wojtal 1996; Watters et al. 2000). For terrestrial fault populations formed in uniform rock types, $D_{\max}$ scales with L as a linear function, such that $D = \gamma L$, where γ is a constant determined by tectonic setting and the mechanical properties of the near-surface crustal materials (e.g., Cowie and Scholz 1992a,b).

The D/L relationship of lunar scarps has been estimated using measurements from LROC NAC stereo-derived DTMs of over 40 scarps. Banks et al. (2017) found D_{max} to range from ~ 10 to 390 m for the scarps measured, assuming a range in θ of 25° to 40°. Obtaining γ as a linear fit to the D/L data in a log-log plot of D_{max} as a function of L, the value of γ for the lunar lobate thrust fault scarp population was found to range from $\sim 2.1 \times 10^{-2}$ to $\sim 1.4 \times 10^{-2}$ for $\theta = 25°$ to 40° ($\sim 1.8 \times 10^{-2}$ for $\theta = 30°$) (Banks et al. 2017). The standard deviation of γ is ~0.2–0.3 × 10^{-2} for the range in θ (0.24×10^{-2} for $\theta = 30°$). Roggon et al. (2017) used LROC NAC stereo-derived DTMs and assumed scarps have a uniform far-field back slope to estimate D_{max} for four scarps, which ranged in D_{max} from ~34 to 384 m. This corresponds to a range in γ of 1.7–2.8 × 10^{-2} for $\theta = 30°$. The values of γ for the lunar scarps reported by Banks et al. (2017) and Roggon et al. (2017) are broadly consistent with, but systematically slightly larger than, the pre-LROC value of $\gamma \cong 1.2 \times 10^{-2}$ for $\theta = 30°$ based on only nine scarps (Watters and Johnson 2010).

Values of γ for lunar thrust faults underlying lobate scarps are lower than γ values for typical thrust faults on Earth ($\sim 8.0 \times 10^{-2}$ for $\theta = 30°$) (Watters et al. 2000), higher than estimates of γ for lobate scarp populations on Mars ($\sim 6.2 \times 10^{-3}$ for $\theta = 30°$) (e.g., Watters and Nimmo 2010) and the large-scale scarps on Mercury ($\sim 8.2 \times 10^{-3}$ for $\theta = 30°$) (Watters et al. 2016), but comparable to those determined for more recently discovered small (< 100 m relief) scarps on Mercury ($\gamma \sim 5.4 \times 10^{-2}$ for $\theta = 30°$) (Watters et al. 2016). The greatest influence on differences in γ for thrust faults on these different bodies is likely the amount of accumulated strain that is principally dictated by the tectonic setting and rock type. The order of magnitude difference in γ between the small-scale thrust faults on the Moon and Mercury and large-scale thrust faults on Mercury and Mars may be the result of small, shallow-depth faults forming in near surface, mechanically weak megaregolith (see Watters et al. 2016). The lack of linked and merged thrust fault clusters forming larger lunar faults that extend in length and depth into the stronger mechanical lithosphere is likely due to the relatively small amount of accumulated contractional strain (Watters et al. 2015a, 2016).

4.2. Wrinkle ridges

4.2.1. Morphology and morphometry. Wrinkle ridges are morphologically complex structures that are often composed of a number of superimposed landforms, usually consisting of a broad arch and superposed narrow, asymmetric ridges (Fig. 3a). The arch component is a relatively wide, gently sloping topographic rise that is commonly asymmetric in cross-section (Fig. 3b) and is only clearly distinguishable in high incidence (low sun) angle photographs and images (Strom 1972; Bryan 1973; Maxwell et al. 1975; Watters 1988). The ridge component is usually long, relatively narrow, and often segmented, as well as commonly strongly asymmetric in cross-section. The vergent side of the ridge often changes either along strike or from one ridge segment to the next, and segments may occur in *en echelon* arrangements (see Tija 1970; Watters 1988). The ridge is often superposed on the arch (Strom 1972; Bryan 1973; Maxwell et al. 1975), but the two morphologic elements may also occur independently of one another (Watters 1988; Watters and Johnson 2010). Smaller second- and third-order ridges that flank or cap the larger ridges are common (Watters 1988). A class of wrinkle ridges that most often occur near the margins of the mare basins exhibits large elevation offsets from one side of the ridge to the other (Watters 1988; Golombek et al. 1991; Watters and Johnson 2010), referred to as "elevation offset ridges" or "EO ridges". The basin-interior sides of these ridges are consistently lower in elevation than the basin-exterior sides.

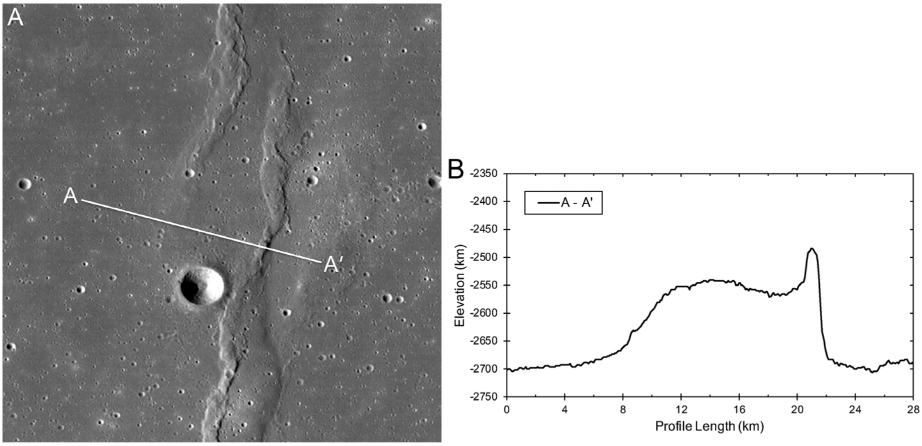

Figure 3. Map view and cross-sectional geometry of the Dorsa Smirnov wrinkle ridge. **A)** Portion of WAC geomorphologic mosaic showing Dorsa Smirnov in Mare Serenitatis. The **white line** shows the location of the topographic profile in 4B. **B)** The profile was extracted from the SLDEM2015 topographic data, and elevations are relative to 1737.4 reference radius. Profile shows morphologic elements of wrinkle ridges, broad arch and superposed ridge. The vertical exaggeration is ~39.

The dimensions of lunar wrinkle ridges vary widely and characterization of their reliefs is complicated by the fact that some mare ridges have very large elevation offsets (Watters 1988; Golombek et al. 1991; Watters and Johnson 2010). The relief of ridges without significant elevation offsets, most of which occur in basin interiors, ranges from tens to hundreds of meters, with measured ridges reaching a maximum relief of ~430 m (Schleicher et al. 2019). Many of the EO ridges have large maximum reliefs, with the largest relief measured on Dorsa Harker in Mare Crisium of ~590 m (Schleicher et al. 2019).

The mean width of the wrinkle ridge population (broad arch) measured by Yue et al. (2015) is 3.7 km, the mean relief is 46 m, and the mean orientation is N358°E, consistent with average orientation calculated by Thompson et al. (2017). The maximum relief of these wrinkle ridges is 610 m, but the majority of ridges have reliefs below 300 m (Yue et al. 2015). Most ridges exhibit NE–SW or NW–SE orientations (Yue et al. 2015).

Watters and Johnson (2010) measured maximum reliefs for several wrinkle ridges using Lunar Topographic Orthophotomaps (LTOs), at a scale of 1:10,000 (Wu and Doyle 1990), and their associated displacements were calculated using these values. To demonstrate the improvement high resolution data makes to previous estimates, updated measurements of a subset of structures have been determined (Table 1) using the LOLA global LDEM, which has a resolution of 118 m/px at the equator. In half of the cases (3 of 6), the improved resolution of the topographic data resulted in an increase in the estimates of the maximum relief and calculated displacement, while in the other half of cases, the updated values were smaller than previously estimated. However, the sum of both the maximum relief and calculated displacements increased, from 1,434 m to 1,445 m and from 2,868 m to 3,190 m, respectively (Table 1). Thus, a small increase in measured relief can result in a substantial increase in calculated displacement, reinforcing the necessity and utility of the recent high-resolution datasets applied to questions regarding basic morphometry of tectonic structures.

Table 1. Dimensions of selected lunar wrinkle ridges.

Ridge name	**Center latitude**	**Center longitude**	**Maximum relief† (m)**	**Maximum relief‡ (m)**	**D† (m), θ = 30°**	**D‡ (m), θ = 30°**
Nicol	18.5° N	22.8° E	240	200	480	400
Lister S	20° N	23.3° E	408	365	816	730
Zirkel	30° N	25.5° W	272	240	544	780
Rubey	9.8° S	42.3° W	48	85	96	170
Smirnov	25° N	25.5° E	300	360	600	720
Von Cotta	25.5° N	12° E	166	195	332	390

Notes:
†Measurements from Watters and Johnson (2010) using topographic data from Lunar Topographic Orthophotomaps (LTOs).
‡This chapter using LOLA data. For more data on lunar wrinkle ridge dimensions, see Watters (2022).

4.2.2. Global distribution. Mapping of wrinkle ridges using new high-resolution image data sets has resulted in two recent maps—those of Yue et al. (2015) and Thompson et al. (2017). Both Yue et al. (2015) and Thompson et al. (2017) mapped wrinkle ridges using the LRO WAC global mosaic with a resolution of 100 m/px as their basemap, while Thompson et al. (2017) also used the GLD100 DTM (Scholten et al. 2012), allowing the identification of more subtle features that may not be visible in imagery alone. The mapping methodologies also differed between the two maps. Thompson et al. (2017) mapped the centerline of each wrinkle ridge structure, while Yue et al. (2015) delineated each ridge segment with a rectangle, where a segment was defined to have similar strike and width. Thus, a single wrinkle ridge structure may be represented either as multiple boxes (Yue et al. 2015) or one polyline (Thompson et al. 2017). These differences in mapping techniques result in differing total numbers of structures mapped: 2839 segments (Yue et al. 2015) versus 5495 structures (Thompson et al. 2017).

Despite the differences in mapping techniques, the geographical distribution of wrinkle ridges in both data sets is similar. Ridges are observed between ±60° latitude, with the majority of structures found between 20–30°S and 50–60°N. Wrinkle ridges are also restricted in longitude, primarily between ~±90°. The largest concentration of wrinkle ridges occurs in NW Oceanus Procellarum. Because wrinkle ridges are confined to the lunar mare (Fig. 4)

(Watters and Johnson 2010; Yue et al. 2015; Thompson et al. 2017), their spatial distribution is limited by the distribution of the mare basalts, and covers ~15% of the near side surface and ~1% of the farside surface (Nelson et al. 2014). The distribution of wrinkle ridges within the mare basalts varies and is strongly related to the boundary geometry that controls the overall shape of the mare deposits (i.e., broadly circular, quasi-circular, or rectilinear). Within the broadly circular mare basins, Imbrium, Serenitatis, Crisium, Nectaris, and Humorum, wrinkle ridges are not evenly distributed, but are more concentrated near the margins than in the central basin (Fig. 4). Within the broadly rectilinear mare regions of Procellarum and Frigoris, ridges are more evenly distributed throughout the mare basalts (Fig. 4). This is also the case in the more irregular, quasi-circular mare basins (Tranquillitatis, Fecunditatis, and Nubium).

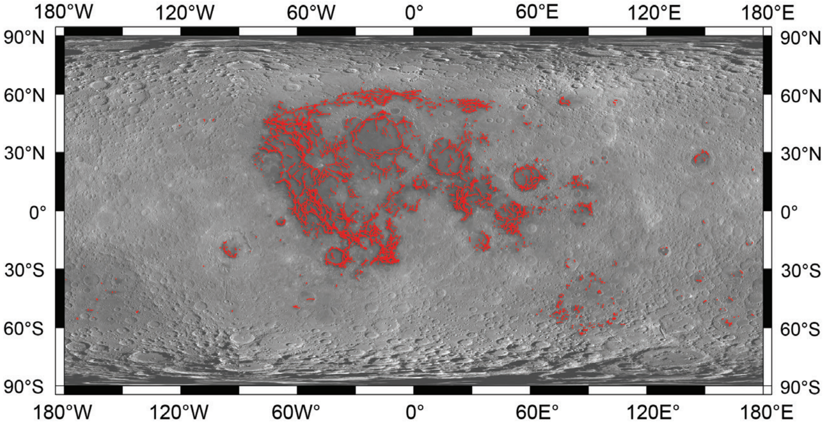

Figure 4. Global distribution of mare wrinkle ridges. Over 5,800 individual wrinkle ridges are mapped (**red lines**) from LROC WAC and NAC images (Thompson et al. 2017). Basemap: LROC WAC global morphologic map, 100 m/px, in equidistant cylindrical projection.

4.2.3. Wrinkle ridge–lobate scarp transitions. Lobate scarps and wrinkle ridges have distinctly different morphologies. As described above, wrinkle ridges are complex structures that may have multiple superposed landforms while lobate scarps are relatively simple morphologically. The fact that both landforms are the surface expression of thrust faults and are thus related tectonic features is clearly demonstrated by the occurrence of wrinkle ridge–lobate scarp transitions (Howard and Muehlberger 1973; Lucchitta 1976; Schultz 1976a; Masursky et al. 1978; Watters 1988; Watters and Johnson 2010). These transitions are most common at contacts between mare and highlands (Fig. 5) and are found in various settings: at the margins of mare basins and rectilinear-shaped mare (e.g., eastern Serenitatis and northwestern Frigoris), at highlands separating mare basins (e.g., Montes Riphaeus), and at small patches of mare separating highland massifs (e.g., Vitello scarp south of Humorum) (Watters and Johnson 2010; Watters et al. 2012; Williams et al. 2019).

The contrast in the morphologic expression of the thrust faults is likely due to the difference in mechanical properties between the mare basalts and the highlands material (Watters 1988), specifically the presence or absence of layering (Watters 1991). Mare basalts consist of a sequence of flows separated by interbeds, while the highlands are mostly mechanically isotropic, lacking discrete layering. A multilayer sequence with mechanically weak layer contacts (i.e., low yield strengths) will have a greater tendency to deform by folding and faulting (Johnson 1980). In contrast to lobate scarps, wrinkle ridges do not show clear evidence of surface-breaking thrust faults. An upward propagating blind thrust fault will induce folding

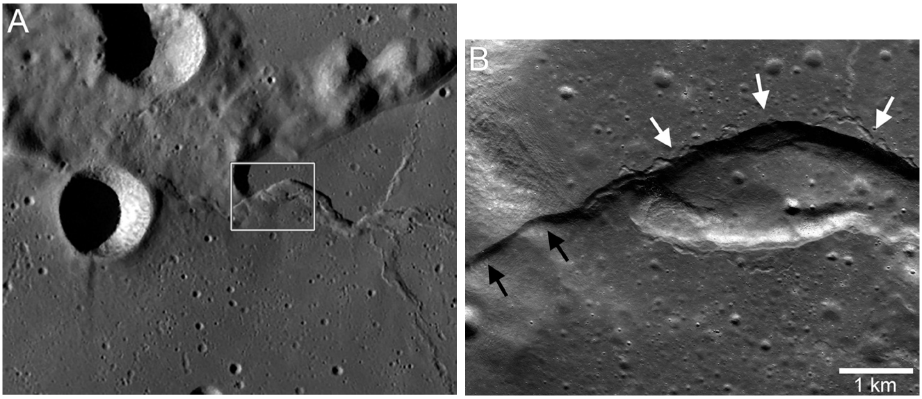

Figure 5. Wrinkle ridge–lobate scarp transition. **A)** The wrinkle ridge transitions to a lobate scarp at the mare–highland boundary in northwestern Mare Frigoris (~60.8°N, 27.1°W) (see Williams et al. 2019). The **box** shows the location of Fig. 5B. **B)** The change in morphologic complexity occurs at the contact between mare basalts and highlands where the wrinkle ridge (**white arrows**) changes to a lobate scarp (**black arrows**). LROC NAC image M188429848R (1.67 m/pixel).

of a multilayer sequence if the layer contacts are weak, while through-going, surface-breaking faulting is favored if layer contacts are strong (Roering et al. 1997; Niño et al. 1998). Slip between flows in the mare basalts probably occurred in interbeds with low shear strengths (Watters 1991), accounting for the more complex morphology of wrinkle ridges. The relatively simply morphology of lobate scarps may be due to the mechanically isotropic behavior of the highlands megaregolith, or if layered, the contacts must therefore be strong and resist slip.

4.2.4. Formation mechanisms. The debate over a volcanic versus tectonic origin for lunar ridges has been replaced by discussions of the relative roles of folding and faulting, the geometry and number of thrust faults, and whether faults are surface breaking or non-surface breaking (blind) (e.g., Golombek et al. 1991, 2001; Watters 1992, 2004; Schultz 2000; Mueller and Golombek 2004). Support for a tectonic origin for mare ridges has been found in subsurface data provided by orbiting radar sounders. Radargrams of the subsurface obtained by the Apollo Lunar Sounder Experiment (ALSE) (Phillips et al. 1973; Maxwell and Phillips 1978; Peeples et al. 1978) and the Kaguya Lunar Radar Sounder (LRS) (Ono et al. 2009) show evidence of anticlinal rises in subsurface horizons and thinning of mare basalt units over structural relief. This demonstrates the importance of subsurface radar sounder data in the study of lunar tectonics. The success of the ground penetrating radar (GPR) instrument on the Chang'E-3 Yutu rover in discriminating layers within Imbrium basalts (Xiao et al. 2015) shows the potential that future rover-based GPRs have to investigate lunar tectonic landforms. Thus, it is generally accepted that lunar and planetary wrinkle ridges are the result of contractional deformation, expressing both folding and thrust faulting, an interpretation further supported by studies of terrestrial analogs, particularly the anticlinal ridges of the Columbia Plateau in the northwestern United States (Plescia and Golombek 1986; Watters 1988; Schultz 2000).

In spite of the consensus on the general formation mechanism of wrinkle ridges, the depth of faulting is debated, specifically whether lunar and planetary wrinkle ridge thrust faults are shallowly ($\lesssim 4$ km) (Watters 1993, 2004; Allemand and Thomas 1995; Watters and Robinson 1997; Mangold et al. 1998) or deeply rooted ($\gtrsim 20$ km) (Zuber and Aist 1990; Golombek et al. 1991, 2001; Tanaka et al. 1991; Zuber 1995; Montési and Zuber 2003a,b; Byrne et al. 2015). Although the class of mare ridges with large elevation offsets are cited as evidence for deeply rooted thrust faults on the Moon (Golombek et al. 1991; Byrne et al. 2015), the majority of ridges either have relatively small elevation offsets that can be accounted for by regional slope

(Sharpton 1992; Watters and Robinson 1997) or no offsets. Evidence cited for shallowly-rooted thrust faults is the apparent sensitivity of wrinkle ridges to be localized by shallow buried landforms, such as interior basin rings and impact craters forming interior ridge rings and ghost craters (Maxwell et al. 1975; Wilhelms 1987; Watters 1988, 1993, 2004; Allemand and Thomas 1995; Watters and Robinson 1997).

4.2.5. Wrinkle ridge boulder fields. One of the surprise discoveries made possible by LROC NAC images are large boulder fields associated with wrinkle ridge that had gone undetected in pre-Apollo and post-Apollo photographs and images (French et al. 2019; Valantinas and Schultz 2020). Blocky wrinkle ridges are generally evenly distributed throughout the mare, with the most prominent boulder fields often found on the steep slopes of the vergent side of the ridges (French et al. 2019). Likely explanations for the boulder fields are that preexisting blocks formed by faulting and folding during initial ridge formation are then exposed by downslope movement of regolith from seismic shaking unrelated to activity on ridge-related thrust faults (French et al. 2019), or blocks are formed and exposed by recent reactivation of ridge-forming thrust faults (Valantinas and Schultz 2020). Evidence of recent tectonic activity in the near side mare is indicated by small-scale wrinkle ridges that are comparable in age to young lobate scarps (Nypaver and Thomson 2022), and may result from the same global stresses thought to be forming lobate scarps.

4.2.6. Displacement–length relationship. From measurement of maximum relief and assuming a planar thrust fault geometry, the displacement has been estimated for many mare ridges (Watters and Johnson 2010; Li et al. 2018). A planar fault geometry, however, does not approximate the ridge-arch cross-sectional morphology of many wrinkle ridges (Watters 2022) (see Fig. 3). Modeling shows a listric fault geometry better accounts for the morphology (Watters 2004, 2022), and $D_{\max}$ for a listric fault can be approximated by scaling the displacement obtained assuming a planar fault geometry D_{lin} by a factor of 2.8 (Watters 2022). A linear fit to estimates of $D_{\max}/L$ for over 98 wrinkle ridges in non-mascon Procellarum and Frigoris and in the mascon basins of Imbrium, Serenitatis, Crisium, and Humorum (using LROC image mosaics and the LOLA-SELENE DEM) yields a value of $\gamma \cong 1.37 \times 10^{-2}$ (Watters 2022). This value of γ is significantly higher than an earlier estimate of $\gamma \cong 6.5 \times 10^{-3}$, assuming a planar fault with $\theta = 30°$ (Watters and Johnson 2010).

The linear scaling relationship between the maximum displacement and fault length of lunar wrinkle ridges (on a log-log plot) indicates that the growth of the thrust faults was not restricted by the thickness of the mare basalt sequences or other influences (see Schultz et al. 2010a). Restricted fault growth can be expressed by nonlinear paths that deviate significantly from unrestricted growth trends (see Soliva et al. 2005). This behavior is evident in the $D_{\max}/L$ relationship of the EO ridges (Watters 2022). The $D_{\max}/L$ values of these ridges do not fall along the trend defined by the population of mare ridges without large offsets. The observed deviation between the two populations of lunar ridges may be the expression of the restricted growth of large EO ridges due to the influence of subsurface basin structure (Watters 2022). The apparent sensitivity of wrinkle ridges to shallow mechanical discontinuities leaves open the possibility that the EO ridges were localized by basin margin subsurface structures that predate mare volcanism and are not the result of deeply rooted thrust faults. Nonetheless, it can be fairly argued that deeply rooted faults created by the impact process have influenced the formation of EO ridges.

4.3. Large-scale graben and extensional structures

4.3.1. Morphology and morphometry. Previously called linear and arcuate rilles, large-scale graben have been long known on the Moon from telescopic observations of its surface, and are distinguished from sinuous rilles that are volcanic in origin (cf. Watters and Johnson 2010). These structures as long, narrow troughs that are either arcuate or linear in plan view with cross-sectional geometry consisting of flat floors and symmetric, steeply dipping inwardfacing walls; based on their geometry, these structures were interpreted to be graben (Baldwin 1963; Quaide 1965; McGill 1971; Lucchitta and Watkins 1978; Golombek 1979). Similar to other planetary tectonic structures, many of these large-scale graben and extensional structures are segmented with *en echelon* steps, indicating that these structures formed through segment linkage (McGill et al. 2000).

The symmetric cross-sectional geometry inferred for most of the graben, as well as the lack of offset of the walls across the structure (i.e., the walls have generally the same relief as they cut through different materials) led to the interpretation that the bounding antithetic faults have roughly similar dips (Watters and Johnson 2010). Based on this interpretation, one kinematic model for lunar graben formation states that the bounding faults intersect at a subsurface discontinuity, commonly assumed to be the megaregolith (Golombek 1979; Golombek and McGill 1983). Assuming a typical normal fault dip angle of 60°, the thickness of the megaregolith can be calculated, and was found to be up to 4 km thick in some places (Golombek 1979).

Two main map-view geometries and one cross-sectional geometry were previously identified: linear and arcuate (e.g., Watters and Johnson 2010) and flat-floored, respectively. However, recent higher resolution imagery and topography has allowed a more detailed investigation of the extensional structures on the lunar surface, resulting in the identification of a more varied array of map-view and cross-sectional geometries than previously described. Nahm et al. (2018) identified four major categories of extensional structures, based primarily on inferred or observed cross-sectional geometry: catena, flat-floored, scarp, and v-shaped. A catena (Fig. 6) consists of a chain of circular to elliptical rimless depressions or pits that are often aligned. A flat-floored structure (Fig. 7a) is a narrow trough with a planar floor and wall that are clearly delineated parallel scarps. These landforms are often segmented. A scarp (Fig. 7b) is an individual or non-paired cliff or escarpment with some elevation offset across the structure. Lastly, a v-shaped structure (Fig. 7c) is a depression with walls converging along the floor, often creating the appearance of a line along it, and thus, forming a “v” shape in cross section. Secondary classifications, based primarily on map-view geometry, have also been defined: linear, arcuate, or elliptical. Structures with deflections (or change in orientation) of 50° or less are defined to be linear, while structures with deflections in excess of 50° are defined to be arcuate (Nahm et al. 2018). Structures with elongate oblong shapes in map view and an enclosing scarp are defined to be elliptical.

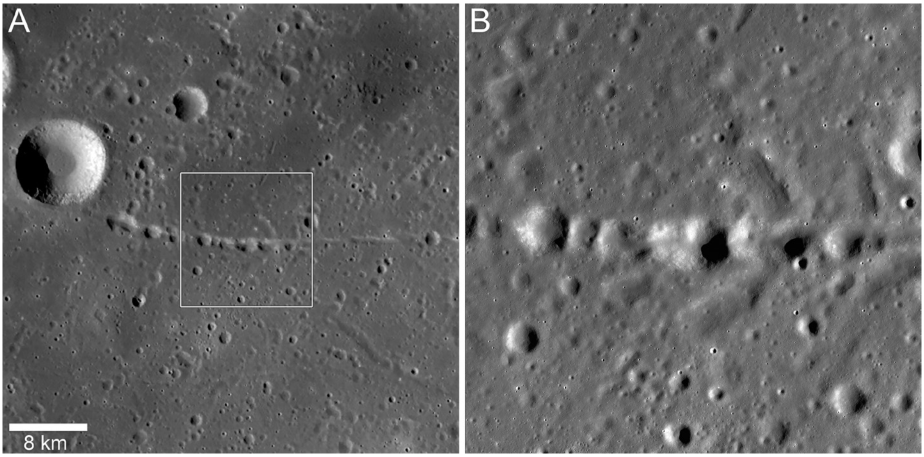

Figure 6. Example of a catena. **A)** The catena is part of a linear graben that extends into Montes Archimedes (26.8°N, 8.5° W). The **box** shows the location of Fig. 6B. **B)** The pits reach depths of more than 300 m. LROC NAC image M1123655039LR (1.34 m/pixel).

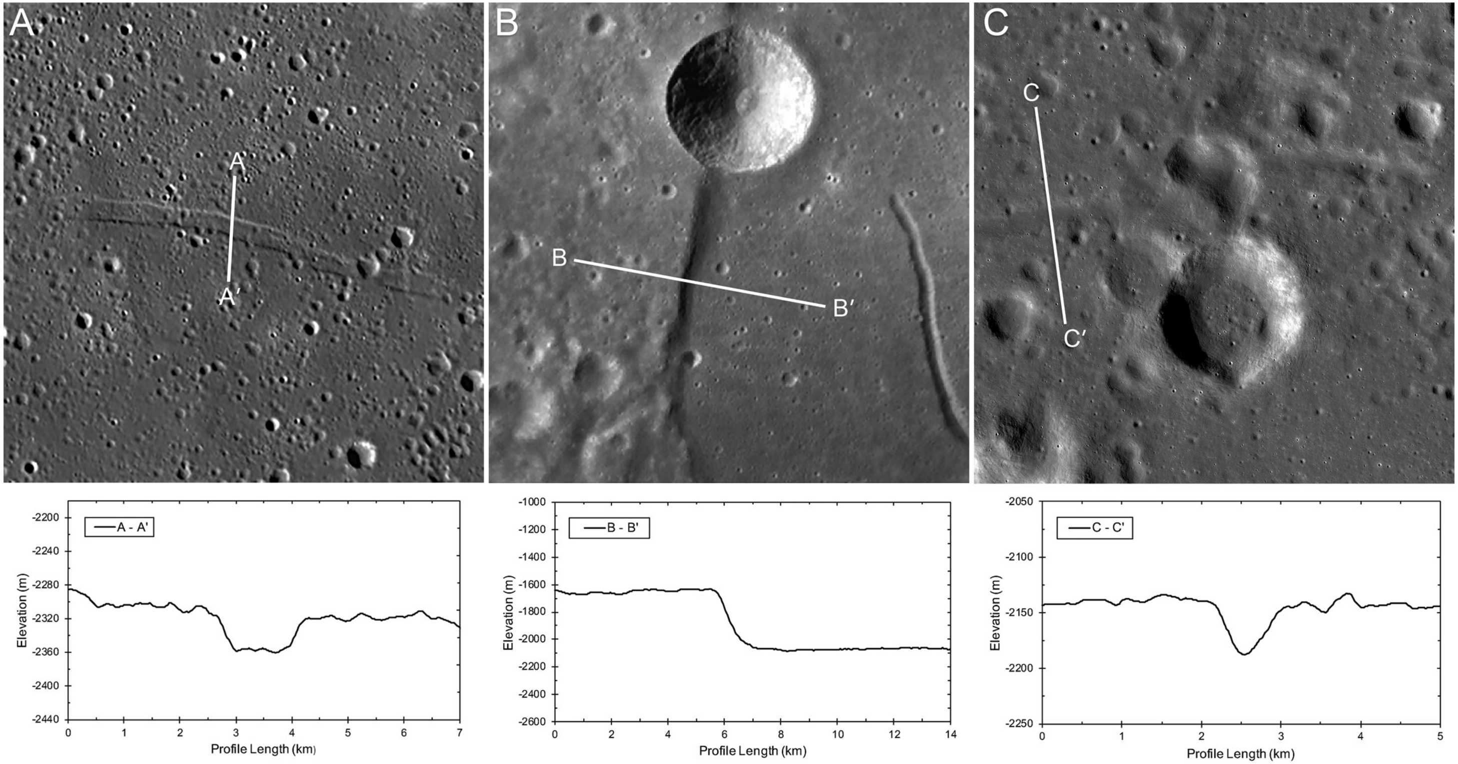

Figure 7. Examples of major extensional structure types and associated topographic profiles. **A)** Flat-floored graben: located at the northern margin of Mare Frigoris (58.7°N, 29.5°E). LROC WAC morphologic global image mosaic. The vertical exaggeration of topographic profile shown in lower plot is ~15. **B)** Normal fault scarp: Rupes Liebig located on the western margin of Mare Humorum (25°S, 45.9°W). LROC WAC morphologic global image mosaic. The vertical exaggeration of topographic profile shown in lower plot is ~6. **C)** V-shaped graben – located near the northwestern margin of Procellarum (49.3°N, 74.0°W). The vertical exaggeration of topographic profile shown in lower plot is ~14. LROC NAC image M1188817612LR (1.34 m/pixel). **White lines** show the locations of topographic profiles shown in lower plots. Topographic profiles were extracted from the SLDEM2015 topographic data, and elevations are relative to 1737.4 reference radius.

A total of ~4,800 extensional structures were mapped with a cumulative length of ~74,000 km (Nahm et al. 2018). The longest mapped structure is ~250 km long, while 96% of structures are 50 km in length or less. The extensional landforms were mapped as polylines composed of multiple segments separated by vertices with segments of roughly equal orientation. The start and end points of a polyline are defined by the visible plan view extent of the extensional trough. The mapped structures show a strongly bimodal distribution of orientations: NE–SW and SE–NW (Fig. 8), consistent with previous maps of a subset of global structures ('lineaments,' i.e., linear structures independent of fault type) (Fielder 1963; Strom 1964; Casella 1976; Chabot et al. 2000), though a N–S orientation previously described by those authors was not identified in the extensional structure map by Nahm et al. (2018).

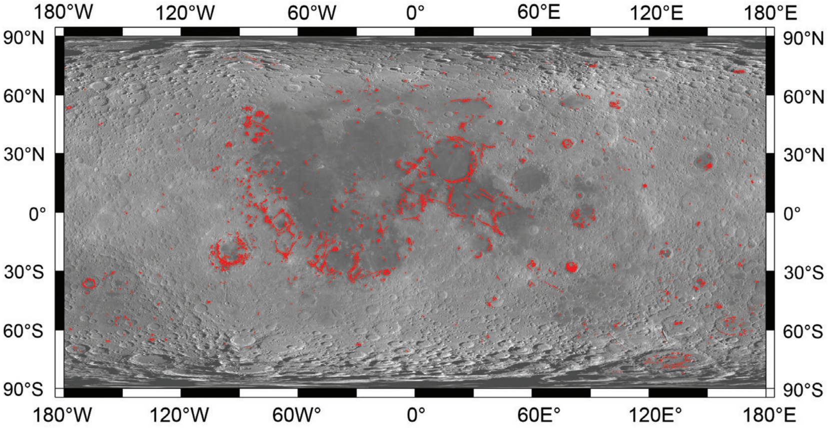

Figure 8. Global distribution of extensional structures. Over 4,800 individual graben are mapped (**red lines**) from LROC WAC and NAC images (Nahm et al. 2018). Basemap: LROC WAC global morphologic map, 100 m/px, in equidistant cylindrical projection

Watters and Johnson (2010) measured maximum depths and widths for several graben using Lunar Topographic Orthophotomaps (LTOs). Assuming a fault dip angle of 60°, the displacements for one of the paired faults were calculated using these depth values. The measured widths are not significantly different between the values determined using LTOs versus those measured with the LROC WAC mosaic (Table 2). Again, updated depth values have been determined (Table 2) using the LOLA global LDEM. In half of the cases (3 of 6), the estimates of the maximum depth and calculated displacement increased, while in the other half of cases, the values were either smaller than or the same as previously estimated. However, the sum of both the maximum depths and calculated displacements increased, from 1270 m to 1660 m and from 1467 m to 1915 m, respectively (Table 2). As was the case for the wrinkle ridges, a small increase in measured relief can result in a substantial increase in calculated displacement, reinforcing the necessity and utility of the recent high-resolution datasets applied to questions regarding basic morphometry of tectonic structures.

4.3.2. Global distribution. Previously thought to exist only on the lunar near side, extensional structures on the Moon are found to be globally distributed (Fig. 8), though the majority of structures (~2/3) occurs on the near side (Watters and Johnson 2010; Nahm et al. 2018). The majority of structure length is concentrated between 40°S and 50°N and 100°W and 40°E (Nahm et al. 2018). Most of these structures are spatially associated with the margins of mare basins (Watters and Johnson 2010; Nahm et al. 2018), though there is a notable lack of structures within and along the margin of Mare Crisium, the northern and eastern margins of Oceanus Procellarum, the northern and western margins of Mare Imbrium, and the southeastern portion of Mare Fecunditatis (Fig. 8; Nahm et al. 2018). Both basin-radial and basin-concentric structures are observed (Quaide 1965; McGill 1971; Golombek 1979; Wilhelms 1987; Watters and Johnson 2010) (Fig. 8), though many structures are located within mare, in the highlands, and on the far side, far from basin margins (Nahm et al. 2018).

Table 2. Dimensions of selected lunar graben.

Graben name	Center latitude	Center longitude	Maximum depth† (m)	Maximum depth‡ (m)	Maximum width† (km)	Maximum width‡ (km)	D† (m), θ = 60°	D‡ (m), θ = 60°
Brackett	17.5° N	23.2° E	230	195	1.71	1.6	266	225
Tetrazzini	26° N	0.6° W	140	175	5.0	4.4	162	202
Patricia	24.8° N	0.5° E	100	90	1.4	1.4	115	104
Bradley	24° N	1° W	400	765	3.25	4.1	462	883
Alphonsus	13° S	1.8° W	120	155	0.8	0.8	139	178
Littrow	22.2° N	29.4° E	280	280	2.25	2.3	323	323

Notes:
†Measurements from Watters and Johnson (2010) using topographic data from Lunar Topographic Orthophotomaps (LTOs).
‡This chapter using the LROC WAC mosaic and LOLA data. Als For more data on lunar graben dimensions, see Martin and Watters (2021), Table 2.

4.3.3. Formation mechanisms. Several mechanisms have been proposed for the formation of graben and extensional structures on the Moon, ranging from local stress sources (e.g., dikes or other igneous intrusions (e.g., Klimczak 2014) to global stress sources (e.g., global expansion (Solomon and Chaiken 1976). Superposition of local basin-related stresses on a global thermal stress field may be responsible for the formation and observed distribution of graben (Solomon and Head 1979). The local stress field is hypothesized to develop in response to loading of the lithosphere by filling and subsidence of mare basins (Solomon and Head 1979). In general, this scenario predicts compressional stresses (and thus, thrust faults) in the basin interior, and extensional stresses (and thus, normal faults) accumulate on the basin margins or exterior to the basins depending on the load geometry (Solomon and Head 1979). The location of peak extensional stresses and graben formation is greatly influenced by the thickness of the elastic lithosphere T_e; the larger the value of T_e the greater the distance of peak extension from the basin center (Solomon and Head 1979, 1980; Watters 2022). The global stress field on which these local stresses are superposed is hypothesized to be thermal stress associated with expansion and contraction of the lunar interior with time (Solomon and Chaiken 1976; Solomon and Head 1979).

This so-called ‘mascon tectonics’ model is generally supported by the observations, namely the presence of wrinkle ridges within basin interiors and concentric graben on basin margins. However, many extensional tectonic structures occur within mare or are not concentric to basin margins (Fig. 8). This observation suggests that the formation of at least a subset of the extensional structures on the Moon was not solely influenced by basin-loading stresses.

An alternative mechanism suggested for graben formation is magma intrusion. Several lines of evidence for the existence of dikes below graben have been discussed in the literature, including magnetic signatures, topographic analysis, and geologic context or associations. A strong linear magnetic anomaly (> 100 nT) was identified in the vicinity of and roughly coincident with Rimae Sirsalis (~15.01°S, 61.36°W) (Anderson et al. 1976, 1977; Srnka et al. 1979; Head and Wilson 1993). The geographic association of a graben with a magnetic anomaly has led to the suggestion that both formed as a result of dike intrusion (Anderson et al. 1976; Srnka et al. 1979).

Deformation of the surface due to dike intrusion is known to cause graben in some cases on Earth (e.g., Pollard and Holzhausen 1979; Pollard et al. 1983; Mastin and Pollard 1988;

Rubin and Pollard 1988; Rubin 1992) and other planetary bodies (e.g., Krassilnikov and Head 2003; Schultz et al. 2004; Head et al. 2009). In dike intrusions, the country rock is displaced up and away from the dike, forming a characteristic topographic signature observable at the surface. Based on this topographic signature, Klimczak (2014) identified a total of 8 graben that are likely to be underlain by dikes. Four of these graben are located within Schrödinger basin (74.73°S, 132.93°E), while the other four (Rimae Daniell [37.53°N, 24.33°E], Rima Hyginus [7.62°N, 6.77°E], Rima Ariadaeus [6.48°N, 13.44°E], and Rima Hesiodus [30.54°S, 21.85°W]) are distributed across the near side close to basin margins. However, recent analysis and modeling by Martin and Watters (2020) suggests there is no definitive evidence of dike involvement in the formation of near side mascon and non-mascon related graben. Analysis of *D/L* relations of near side graben normal faults and their displacement profiles suggests that normal fault growth of graben in the highlands is unrestricted, while normal faults of graben in the mare basalts show evidence of restricted growth (Martin and Watters 2022).

Other intrusive processes have also been invoked to explain the formation of certain extensional features on the Moon, particularly in the context of fractures within floor-fractured craters (FFCs). Ascending magma stalls in the low-density zone below the FFC floor, forming a sill, which inflates to form a laccolith (Schultz 1976b; Head and Wilson 1979; Jozwiak et al. 2012; Wilson and Head 2018). The laccolith inflation forms fractures in the overlying crater floor and favors magma ascent, which, in some cases, results in subsequent eruption (effusive, explosive, or both). This hypothesis is supported by the observation that lunar pyroclastic deposits and/or lava often occur within FFCs (e.g., Head and Wilson 1979; Coombs et al. 1992; Gaddis et al. 2003; Wilson and Head 2018), such as within Lavoisier crater (38°N, 81°W) (Coombs et al. 1992) or Gassendi crater (17.55°S, 39.96°W) (Schultz 1976b).

Some extensional structures have pit chains associated with them, such as Rima Hyginus (~7.62°N, 6.77°E). Pit chains may form volcanically by localized explosive venting of gas exsolved from magma at depth (Wilson and Head 1996, 2018) or are expressions of dilational normal faulting (e.g., Ferrill and Morris 2003; Grant and Kattenhorn 2004), in which draining of unconsolidated regolith into the subsurface may occur, as proposed for Mars (e.g., Ferrill et al. 2004, 2011), Enceladus (e.g., Michaud et al. 2008; Martin et al. 2017), and, recently, the Moon (Xiao et al. 2010).

4.4. Small-scale graben

4.4.1. Morphology and morphometry. NAC images have revealed previously undetected small-scale graben associated with lobate scarps and wrinkle ridges (Fig. 9; Watters et al. 2010). The small-scale graben have relatively steeply sloping walls and flat floors (Watters et al. 2010) and are typically oriented parallel or perpendicular to the strike of the scarp or ridge (Watters et al. 2010; French et al. 2015). It is generally assumed that the graben are bounded by symmetric antithetic normal faults with fault dip angles of ~60°, typical for normal faults, and that they are rooted or extend to the base of the regolith (Watters et al. 2010; French et al. 2015).

Larger small-scale graben, such as the Vitello graben (lengths up to 600 m and widths up to 15 m), exhibit *en echelon* steps (Watters et al. 2012), indicative of growth by segment linkage (e.g., Schultz et al. 2010b). Pit chains occur in the Vitello graben as well as other small-scale graben (Watters et al. 2012; French et al. 2015). These pit chains exhibit depressions that are circular to elliptical in map view and may span the entire width of the graben (Watters et al. 2012). The Virtanen graben consist of closely spaced and overlapping segments and exhibit complex fault linkages (Watters et al. 2012). The constituent faults are often segmented and some are linked by relay ramps (downward-sloping landforms bounded by two adjacent, overlapping normal faults: Watters et al. 2012).

Lengths, maximum widths, and orientation of 238 small-scale graben were measured (French et al. 2015). The orientation of graben with respect to ridges and scarps varies; in some

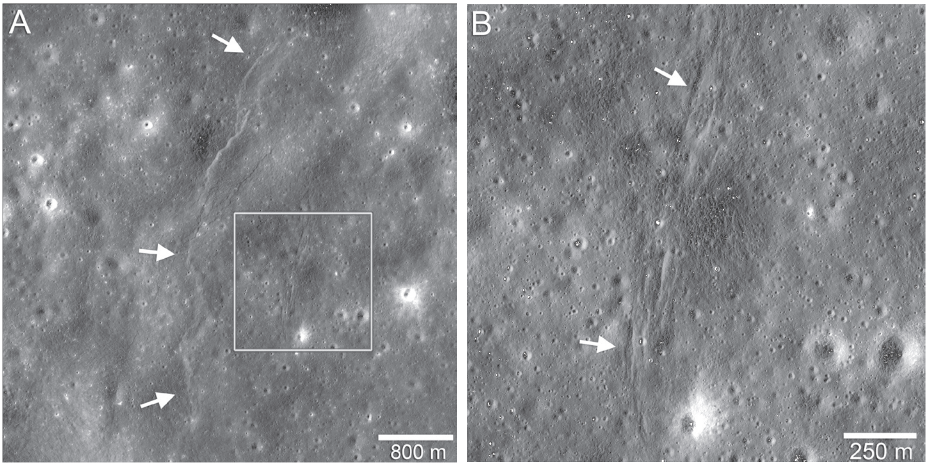

Figure 9. Small-scale graben associated with lobate scarp. **A)** Pasteur scarp (**white arrows**) has maximum relief of ~20 m and is located in nearside highlands (~ 8.6°S, 100.6°E). LROC NAC frame M103854211L. B) Small graben oriented parallel to the scarp face are found ~1.2 km in the back-scarp terrain (**white arrows**). Location of 9B is shown by the box in 9A (after Watters et al. 2015). LROC NAC image M1113517026LR (1.05 m/pixel).

cases the graben change from ~perpendicular to ~parallel to the main structure within a single group (Watters et al. 2010; French et al. 2015). Graben widths vary from 5 to 56 m, while the mean width of the small-scale graben is 26 m and the median is 15 m, representing the presence of the larger graben sets (French et al. 2015). Graben lengths have a mean of 179 m and a median of 139 m (French et al. 2015). The mean graben spacing is 76 m, determined from 158 graben (French et al. 2015).

Differences in small-scale graben morphometry are observed between those in the highlands and those in the mare (French et al. 2015). In general, graben lengths and widths are larger for structures in the highlands versus the mare (French et al. 2015), perhaps representing a difference in material strength. In addition, graben associated with either lobate scarps or wrinkle ridges are smaller (both width and length) than those independent of larger structures (French et al. 2015).

Dozens of small-scale graben have been identified in an area of locally high relief in the southeastern portion of the ejecta blanket of Copernicus crater (French et al. 2015; Xiao et al. 2017). This system is over 7 km long and 3 km wide, though most graben are shorter than 1 km; graben widths range from 10 to 400 m (French et al. 2015; Xiao et al. 2017). The graben system strikes NW–SE (Xiao et al. 2017). Based on photoclinometry, individual scarps have been determined to be 1 to 10 m high (Xiao et al. 2017). The bounding faults of the graben system exhibit right lateral *en echelon* steps, suggesting a component of right lateral slip (Xiao et al. 2017). These small-scale graben crosscut craters that superpose the ejecta deposit, implying that the tectonic activity here is Copernican (French et al. 2015; Xiao et al. 2017).

4.4.2. Global distribution. Small-scale graben are distributed globally (Fig.10), but are slightly more prevalent in or close to the near side mare. These structures are observed largely near lobate scarps in the highlands and wrinkle ridges in the maria, though several graben groups are not located near a scarp or ridge (French et al. 2015). Small-scale graben, such as those in the back-limb area of the Lee-Lincoln scarp, are often spatially correlated with a narrow topographic rise along the scarp crest (Watters et al. 2012). In the cases where the graben are not related to a scarp or wrinkle ridge, they may form in locally low-lying areas, such as the graben on the floor of Seares crater (Watters et al. 2012), or local high-relief areas, such as in Mare Humorum near the Vitello crater (Watters et al. 2012; French et al. 2015).

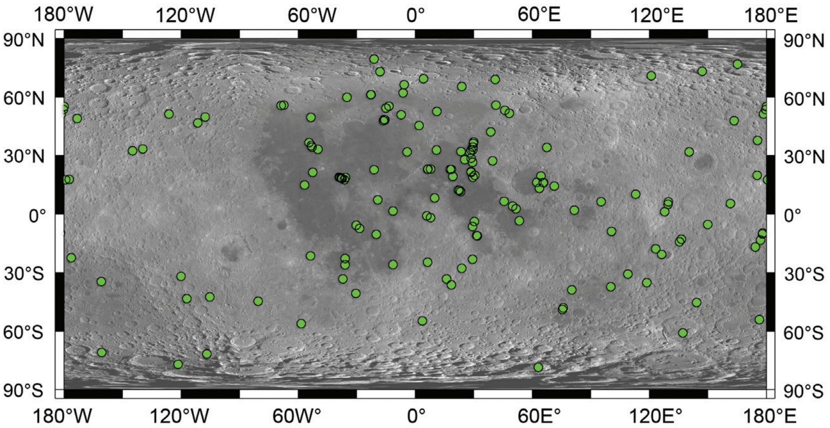

Figure 10. Global distribution of small-scale graben. The map shows the locations (**green circles**) of over 100 small graben detected thus far (French et al. 2015). Basemap: LROC WAC global morphologic map, 100 m/px in equidistant cylindrical projection

4.4.3. Formation mechanisms. Some small-scale graben are interpreted to have formed as a result of regolith and bedrock extension as a result of flexural bending of the thrust fault hanging wall (Watters et al. 2010; Watters et al. 2012; French et al. 2015). During fault slip, bending stresses cause extensional stresses and resultant normal faulting in the near-surface regolith and crust of the back-limb area (Watters et al. 2010; French et al. 2015). These bending stresses may have locally exceeded the background compressional stress, limiting extension to the back-limb areas of lobate scarps and wrinkle ridges (Watters et al. 2012).

In several cases, graben sets occur between *en echelon* wrinkle ridge segments, likely forming from dilation of the regolith as the ridge segments slipped (French et al. 2015), while other small-scale graben (e.g., in Seares crater) may have formed as a response to extensional stress as dilation occurred surrounding the developing lobate scarps (Watters et al. 2012). In addition, the occurrence of pit chains at several graben is evidence for dilational normal faulting (Ferrill and Morris 2003), in which extension allows drainage of loose regolith material into a subsurface void.

Shallow magmatic intrusion may be responsible for the formation of small-scale graben in cases where they are not associated with contractional structures (French et al. 2015). The larger of the small-scale graben sets (Copernicus, Numerov, and Virtanen) are independent of contractional tectonic landforms and are likely not confined to the upper regolith layer, suggesting a formation mechanism separate from the majority of the smaller small-scale graben (Watters et al. 2012; French et al. 2015). For example, these small-scale graben may have formed as a result of localized uplift from shallow intrusions such as laccoliths or dikes (Watters et al. 2012; French et al. 2015; Xiao et al. 2017).

4.5. Structures without surface expressions

4.5.1. Deep-seated structures observed in GRAIL data. The earliest tectonic evolution signatures of the Moon are of great interest and have important implications for early lunar evolution. However, while tectonic structures formed since the Imbrian period are often well preserved and clearly expressed at the surface, structures dating back to the Pre-Nectarian, Nectarian, and early Imbrian epochs are often hidden from view by the effects of subsequent resurfacing by impacts and volcanism. Nevertheless, lasting subsurface density anomalies associated with faulting can be preserved even after the surface record is lost and can in some cases be detected in gravity data. Such density anomalies can arise when faults offset a density interface in the subsurface, when structures are associated with dense intrusions of igneous material, or when surface structures are flooded by dense lava. For this purpose, dikes are considered here to be tectonic structures, since the orientation and opening of the dike is often controlled by regional stresses. A dike is a mode I (opening) fracture accompanied by or caused by an intrusion of magma. Moreover, dikes are often accompanied by tectonism at the surface (Rubin 1992), and lunar dikes have been interpreted to underlie some graben (see Section 4.3.3) (Head and Wilson 1993; Wilson et al. 2011; Klimczak 2014).

Data from the GRAIL mission (Zuber et al. 2013b; Konopliv et al. 2014; Lemoine et al. 2014) provided the ability to reveal density anomalies associated with ancient tectonic structures in the subsurface. GRAIL gravity models have been made to spherical harmonic degree and order 1200 (corresponding to a half-wavelength resolution of 4.5 km), though the data begins to show signs of noise and orbit-parallel striping beyond degree 600 (half-wavelength resolution of 9 km). In practice, pervasive small-scale variability in the gravity field due to variations in the near-surface density and porosity of the crust (Jansen et al. 2017) makes detecting structures near the limit of resolution of the data difficult. Nevertheless, the GRAIL data have revealed a number of large-scale ancient tectonic structures that shed light on the early evolution of the Moon. Other features revealed by GRAIL are basin ring structures (Zuber et al. 2013b). Basin rings buried by mare basalts may have a significant influence on localizing wrinkle ridges (see Section 4.2.4).

A number of randomly oriented linear gravity anomalies with lengths up to 1000 km were first identified in GRAIL gravity gradients (second horizontal derivatives of the Bouguer gravity field) (Andrews-Hanna et al. 2013). These anomalies are distributed across the entire globe including the most ancient terrains and lack any surface expression. The pattern and magnitude of the anomalies is most simply explained by the presence of large-scale dike-like intrusions in the subsurface, with modeled widths typically in the range of 4–30 km (Andrews-Hanna et al. 2013). Individual structures may represent single large-scale intrusive bodies, analogous to the intrusions associated with collapse pits near Valles Marineris on Mars (Mège et al. 2003). Alternatively, individual gravity lineations may represent tightly clustered linear swarms of unresolved smaller dikes (Ernst et al. 2001). In either interpretation, substantial horizontal extension is required to accommodate the intrusions. By analogy with dike swarms and intrusions on other planets (e.g., Head and Wilson 1993; Ernst et al. 2001; Wilson and Head 2002; Mège et al. 2003), one can infer that these ancient lunar structures would have formed in combination with rifts, graben, and/or collapse pits at the surface. The lack of surface expression accompanying the gravity anomalies indicates that the associated structures must pre-date the surfaces beneath which they are found, which in many cases are Nectarian or pre-Nectarian in age. Thus, the ancient igneous intrusions record an episode of pre-Nectarian magmatic-tectonic activity.

Sawada et al. (2016) studied 20 ‘probable’ linear gravity anomalies (LGAs) to determine whether or not an associated surface expression could be observed. A subtle long wavelength surface depression (up to 400 m in relief) is observed in LOLA topography above 17 of the 20 studied LGAs, confirming that these structures likely formed as a result of horizontal extension (Sawada et al. 2016). Crater counting on the surface in the vicinity of individual LGAs indicates formation prior to 4.1 Ga (Sawada et al. 2016), consistent with the timing inferred for LGAs by Andrews-Hanna et al. (2013).

Another set of ancient structures is revealed on the lunar near side bordering the Procellarum region (Andrews-Hanna et al. 2014). These structures also consist of largely linear gravity anomalies, but they differ in several key respects from the ancient igneous intrusions described above. Most notably, the Procellarum border structures circumscribe a quasi-rectangular pattern, comprised of nearly linear structures along its sides, intersecting at sharp angles. The structures are larger in scale, with widths on the order of 100 km. The gravity anomalies are associated with mare-flooded depressions in the feldspathic crust, most clearly manifest in the structure beneath the arcuate Mare Frigoris.

4.5.2 Formation mechanisms. The population of structures interpreted as ancient igneous intrusions are randomly oriented and show no evidence for control by any known or hypothesized stress fields, including tidal-rotational stresses from the early orbital evolution of the Moon (Matsuyama and Nimmo 2008; Andrews-Hanna et al. 2013; Keane and Matsuyama 2014). Rather, the structures are most simply interpreted as forming through magmatism in an isotropic extensional stress field as could arise from expansion of the interior. The length and widths of the inferred intrusions lead to estimates of interior expansion by 0.6–4.9 km (Andrews-Hanna et al. 2013). Sawada et al. (2016) also estimated the expansion implied by the topographic lows associated with a small subset of LGAs, obtaining somewhat lower values of 50 m–0.5 km. Combined with the inferred early timing of these features, the results suggest an early period of global expansion not heretofore observed.

The gravity anomalies bounding the edge of the Procellarum region are consistent with the interpretation of these structures as volcanically flooded ancient rift zones, buried beneath the near side maria (Andrews-Hanna et al. 2014). This interpretation is supported by the arcuate pattern of some structures resembling arcuate half graben in rift zones, as well as the intersections of structures at 120° angles similar to triple junctions of terrestrial rift zones. Models of the subsurface crustal structure associated with the border anomalies are consistent with crustal thinning driven by extension of 8–18 km. This interpretation is noteworthy, since similar rift zones have been documented on the Earth, Venus, and Mars (e.g., Nimmo 2004; Kiefer and Swafford 2006; Hauber et al. 2010), but large-scale rifting and thinning of the lunar crust has not been previously documented. More recent extension and normal faulting on the Moon is much smaller in scale and likely confined to the upper crust (Watters et al. 2012). Scenarios that might predict both the early global expansion and the localized buried rift zones around the Procellarum terrain are discussed in Section 6.

4.6. Lunar seismicity

During the Apollo missions to the lunar surface, a network of four passive seismometers were installed at the 12, 14, 15, and 16 landing sites, and this network continually monitored the Moon for seismic signals from 1969 to 1977. During this period of operation, over 12,000 seismic signals were detected (Nakamura et al. 1981). Naturally-occurring seismicity on the Moon was found to consist of four primary types: meteorite impacts, thermal moonquakes, shallow moonquakes, and deep moonquakes.

Thermal moonquakes are extremely small, local high-frequency signals associated with lunar sunrise and sunset, probably representing the thermal "pinging" and cracking of regolith, rocks, and crater walls in the immediate vicinity of the landing site, and possibly including the lunar lander itself (Duennebier and Sutton 1974; Weber et al. 2017).

Over 6000 deep moonquakes were recorded. Their epicenters were found to be distributed over much of the near side, with a few just beyond the limb on the far side. The deep moonquakes were observed to originate from discrete source regions, called clusters, at depths between ~750 and 1200 km (Nakamura 2005). Deep moonquakes occur with tidal periodicity, suggesting that they are either triggered or caused by the buildup and release of tidal stress (Weber et al. 2010; Kawamura et al. 2017). Their mechanism is not completely understood, since brittle failure is not expected at the temperature and pressure conditions at that depth (ductile regime). Some proposed hypotheses include phase-change-induced transformational faulting and dehydration embrittlement (Frohlich and Nakamura 2009).

Shallow moonquakes were comparatively rare. The signal characteristics of the 28 shallow moonquakes recorded by Apollo seismic network distinguish them from deep moonquakes and seismic activity caused by impact events (Nakamura 1977, 1980; Nakamura et al. 1979). The shallow moonquakes occur at depths generally constrained to be less than 100 km and are the most energetic recorded seismic events (Nakamura et al. 1979; Nakamura 1980).

4.6.1. Relationship to tectonic structures. The combination of inferred shallow moonquake depths and their released energy led Nakamura (1980) to conclude that the shallow moonquakes are similar to tectonically-generated intraplate earthquakes. The spatial correlation of some shallow moonquakes with the edges of mare basins suggests that the inferred tectonic activity might be basin-localized (Nakamura et al. 1979; Nakamura 1980). The discovery of the globally distributed population of young thrust fault scarps has greatly expanded the number of possible tectonic landforms that could be connected with the recorded shallow seismic activity.

Lobate thrust fault scarps are the youngest and most widely distributed tectonic landforms on the Moon (Fig. 2; Section 4.1; Binder and Gunga 1985; Watters et al. 2010, 2012, 2015a; van der Bogert et al. 2018). A direct comparison of locations of the shallow moonquakes with mapped fault scarps is hindered by the large uncertainty of the epicentral locations that may be only accurate to several degrees, perhaps greater for smaller, more distant events. Using clouds of relocated candidate locations generated by an algorithm adapted for inaccurate data from sparse seismic networks, 8 out of 17 epicenters with surface solutions fall within 30 km of a mapped lobate scarp, the distance over which shake models predict strong ground shaking, with the closest < 4 km from a scarp (Watters et al. 2019). To show that the proximity of the 8 relocated epicenters is not a random effect, Monte Carlo tests with 10,000 sets of 17 randomly-generated epicentral locations indicate that less than 4% of the random locations occur within 30 km of a lobate scarp and none of the 10,000 sets have more than 5 quake locations within 30 km of a scarp (Watters et al. 2019). Further, 7 shallow moonquakes with epicenters within 60 km of a fault scarp occur when the Moon was near-apogee, the time stress models predict peak compressional stresses. Thus, the proximity of young lobate scarps to relocated epicentral locations with surface solutions and the timing of the events supports the hypothesis that the shallow moonquakes are due to slip events on scarp-related thrust faults.

Finally, although it is unlikely that a quake occurring at the depths of deep moonquakes would have a surface expression, they have been suggested to coincide with the locations of mare basalts (Watters and Johnson 2010; Qin et al. 2012), also possibly linking their origin to the presence of volatiles that weaken rocks under pressure.

4.6.2. Evidence for recent seismic activity. Seismic shaking of the lunar regolith is a direct consequence of shallow moonquakes. Manifestations of this might include disturbed regolith on relatively steep slopes, landslides, and boulder movement (Watters et al. 2010, 2019; Kumar et al. 2016, 2019). Seismically-induced downslope creep or landslides should expose fresh material with a higher albedo than the surrounding regolith that has been darkened by space weathering (Watters et al. 2019). Another phenomenon related to seismic shaking is local resetting of the population of small-scale impact craters (van der Bogert et al. 2018).

Boulders in close proximity to lobate scarps on the Moon are common (Watters et al. 2010, 2019; Kumar et al. 2016, 2019). Perhaps the best known are the Apollo 17 Station 6 and 7 boulders that are located on the slope of North Massif, only about 5 km from the Lee-Lincoln scarp that cuts across the Taurus-Littrow valley (see Arvidson et al. 1975). Other boulders are concentrated along a segment of the scarp face of Lee-Lincoln where it extends into the highlands of North Massif (Watters et al. 2010).

Lobate scarps identified in Schrödinger basin and Laue crater have been associated with numerous boulder falls (Kumar et al. 2016, 2019). Boulder fall populations in Schrödinger and Laue exhibit boulders without trails or bounce marks and boulders with one or both characteristics (Kumar et al. 2016, 2019). It is suggested the boulder falls in Laue are due to seismic shaking from a recorded shallow moonquake with an epicenter estimated by Nakamura et al. (1979) to be located on the northwestern interior wall of the crater (Kumar et al. 2019). A relocated epicenter of this shallow moonquake has a surface solution located just outside the northeastern rim of Laue (see Watters et al. 2019), approximately 80 km from the most prominent lobate scarp in the crater, supporting a possible connection between the boulder falls and the shallow moonquake.

Movement of boulders from coseismic slip events is not restricted to falls and rolls on slopes on or nearby lobate scarps. Boulder fields are usually associated with patches of relatively high albedo regolith and may indicate very recent downslope movement of regolith exposing the boulders due to seismic shaking (Watters et al. 2019). Boulders within a degraded crater located in the back-scarp terrain that are aligned in rows paralleling the orientation of the scarp are further evidence of the effects of shaking induced by coseismic slip on scarp-related thrust faults (Watters et al. 2019).

The accumulation of structural relief on lobate scarps is expected to involve many coseismic slip events on associated thrust faults. The effect of multiple episodes of seismic shaking might be expressed in the degradation state of craters, which could result in an under-represented or missing range of small-diameter craters in crater size–frequency distributions (CSFDs) proximal to lobate scarps relative to CSFDs in areas distant from the scarps. In an analysis of five lobate scarps, van der Bogert et al. (2018) show that fault slip events may affect crater populations with craters up to 100 m in diameter and that surface renewal occurs both adjacent to and kilometers away from scarps.

5. TIMING OF TECTONIC STRUCTURE FORMATION

The relative and absolute ages of the different classes of tectonic structures on the Moon are important to understanding the timing of tectonic stresses (and their sources). Typically, absolute ages of tectonic structures are constrained by determining the ages of the units that they deform (Watters and Johnson 2010). Work from the 1970s suggested that large-scale extensional tectonics associated with lunar maria ceased on the Moon around 3.6 Ga (Boyce 1976; Lucchitta and Watkins 1978), though as discussed below, our recent understanding of ages of extensional structures has changed this view somewhat. Wrinkle ridges deform the youngest basalts on the Moon, dated to be 1.2 Ga (Hiesinger et al. 2003), as well as the oldest basalts (Watters and Johnson 2010). This suggests that crustal shortening associated with the lunar maria occurred at least as recently as 1.2 Ga.

The results of tectonic mapping enabled by recent missions, including the identification of subsurface structures with no surface expression and previously undetected types of structures, has implications for the understanding of the evolution of lunar stresses and their resultant tectonic activity. First, results from the GRAIL mission have provided new evidence of the earliest lunar tectonic activity (see Section 4.5), likely extension related to early expansion, as well as the formation of the Procellarum region. Second, the duration and interplay of tectonism in the lunar mare, while still similar to previous interpretations, is known in more detail (see Sections 5.1 and 5.2.2). Third, there is a variety of lines of evidence for recent tectonic activity (see Section 5.3), perhaps even reflected in the present-day lunar seismicity (see Section 4.6).

5.1. Relative ages of structures

Based on previous work regarding the absolute ages of tectonic structures, basin-related graben are older than ~3.6 Ga (Lucchitta and Watkins 1978) and some wrinkle ridges are nearly as old as the oldest mare basalts (~4 Ga) with some ridges younger than the youngest mare basalts (~1.2 Ga) (Hiesinger et al. 2003). A recent survey of globally-distributed crosscutting relationships between large-scale graben and wrinkle ridges (Nahm et al. 2016) indicates that of the 33 cases examined, most crosscutting relationships show that graben are older than wrinkle ridges. However, in 5 cases, this relationship is reversed (Nahm et al. 2016). The cases where the wrinkle ridges pre-date the graben are located at the margins of Mare Vaporum, Mare Serenitatis, and Mare Humorum. These cases indicate that more detailed study into both the relative and absolute timing of difference classes of tectonic structures is important to understand the evolution of tectonic stresses.

5.2. Absolute ages from crater counting

5.2.1. Lobate scarps and associated small-scale graben. Lobate scarps are interpreted to be very young, among the youngest tectonic landforms on the lunar surface (Schultz 1976a; Binder and Gunga 1985; Watters and Johnson 2010; Watters et al. 2010). Watters et al. (2010) assigned a Copernican age to lunar scarps because many scarps cross-cut craters < 50 m in diameter, which themselves are estimated to be Copernican based on their expected degradation lifetime (Trask 1971). Absolute model ages (AMAs) derived from buffered and traditional CSFD measurements at lunar lobate scarps also support a late Copernican age. Ages derived for several lobate scarps vary depending on the location of the measurement area. For the hanging wall of Mandel'shtam (5.67°N, 161.62°E), AMAs are ~91, 128, and 307 Ma, while the AMAs for the footwall are ~146 and 372 Ma (van der Bogert et al. 2012). Similarly, the AMA for the hanging wall is younger than the footwall for the Lee-Lincoln (20.27°N, 30.56°E) scarp, with the hanging wall dated to be ~76 Ma and the footwall dated to be ~91 Ma (van der Bogert et al. 2012). Using the method developed by van der Bogert et al. (2012), Clark et al. (2017a) dated both the hanging walls and footwalls for five additional lobate scarps: Joy (25.28°N, 6.84°E), Barrow A (69.89°N, 4.73°E), Wilsing Z (20.36°S, 156.16°W), Romer P (26.45°N, 39.78°E), and Plummer C (23.5°S, 153.09°W). The AMAs derived for the hanging walls of these scarps range from ~86 Ma (Plummer C) to ~132 Ma (Wilsing Z), while the AMAs for their footwalls range from ~54 Ma (Wilsing Z) to ~210 Ma (Barrow A) (Clark et al. 2017a). Also following the method from van der Bogert et al. (2012), van der Bogert et al. (2018) dated the hanging walls and footwalls for five lobate scarps: Henderson 2 (7.77°N, 152.07°E), Kondratyuk (15.03°S, 116.78°E), Koval'skiy 3 (20.9°N, 102.6°E), Mandel'shtam 3 (5.83°N, 161.03°E), and Morozov (6.54°N, 129.94°E). AMAs for the hanging walls of these structures range from ~79 Ma (Kondratyuk) to ~1.0 Ga (Mandel'shtam 3), while the AMAs for their footwalls from ~56 Ma (Kondratyuk) to ~1.1 Ga (Koval'skiy 3) (van der Bogert et al. 2018). The differences in the AMAs derived for the hanging walls and footwalls of lobate scarps is interpreted to represent seismic resetting of the CSFDs (van der Bogert et al. 2012, 2018), implying that these scarps were active as recently as their youngest derived AMAs (Clark et al. 2017a). Using buffered crater counting, Kumar et al. (2016) determined the ages for 4 lobate scarps within Schrödinger basin to be between ~11 and 82 Ma. In summary, the ages for 15 different locate scarps across the Moon have reported AMAs < 150 Ma.

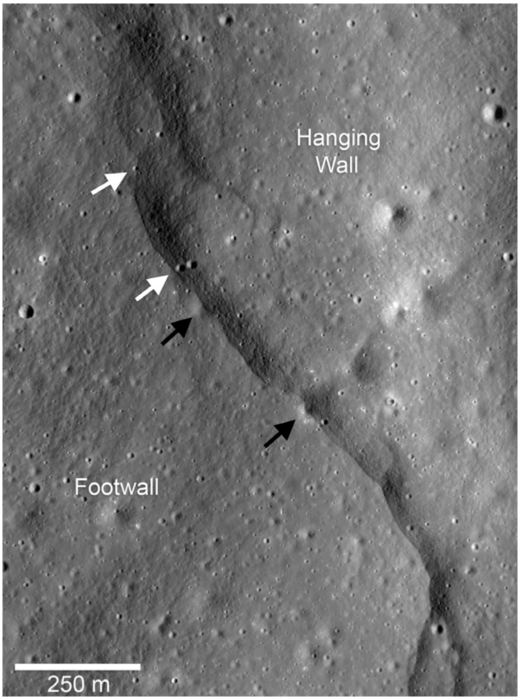

Figure 11. A section of the Mandel'shtam-3 scarp segment. Lobate scarps are observed to cross-cut small craters (**black arrows**) and are also cross-cut by small craters (**white arrows**) (after van der Bogert et al. 2018). LROC NAC image M191909925LR (1.27 m/pixel).

Additional support for the very young age for all the lobate scarps is their consistently crisp, undegraded morphology (Binder and Gunga 1985; Watters et al. 2010; Fig. 11).

Furthermore, the small-scale graben associated with some scarps are also interpreted to be very young; they cut meter-scale craters, have crisp and undegraded appearances, and are expected to have short (tens of Ma) degradation lifetimes (Watters et al. 2012, 2015a; French et al. 2015).

5.2.2. Wrinkle ridges. Absolute model ages derived from buffered CSFD measurements for mare wrinkle ridges across the Moon indicate they have ages that range from 3.5 to 2.4 Ga (Yue et al. 2017). The oldest wrinkle ridges are located within Fecunditatis and Crisium, with model ages of ~3.5 Ga, while the youngest, dated to be 2.4 Ga, occur in Tranquillitatis (Yue et al. 2017). The dated wrinkle ridges formed between 100 Myr (in Crisium) and 1.4 Gyr (in Tranquillitatis) after the formation of the mare units within which the ridges are contained, though most are 100 to 650 Myr younger (Yue et al. 2017). In a study based on subsurface stratification observed in radar data from Mare Serenitatis, Ono et al. (2009) inferred that ridges there are younger than 2.84 Gyr, much younger than the 3.4 Ga age obtained for these ridges by Yue et al. (2017).

Details now revealed in LROC NAC images also suggest more recent activity at some mare wrinkle ridges. For example, a population of morphologically crisp wrinkle ridges was identified in Mare Frigoris (Williams et al. 2019). These wrinkle ridges in western Frigoris have relatively steep slopes, few superposed large craters (>400 m in diameter), and crosscut small craters (<100 m diameter) (Williams et al. 2014, 2016). This ridge population was found to exhibit not only morphologic but also stratigraphic evidence for recent formation or reactivation, and some ridges have associated small-scale graben, morphometrically and morphologically similar to the small graben associated with some highland lobate scarps. Previous work (see Section 4.1) has suggested that lobate scarps may be as young as 50 Ma (Watters et al. 2015a) and that small-scale graben may have formed within the last 50–100 Myr (Arvidson et al. 1975; Watters et al. 2012). Thus, the presence of these small graben implies that not only are they very young, but also that the wrinkle ridge faults causing the associated flexure resulting in their formation must have been active within the past few tens of millions of years, and indeed could still be active today. An additional study showed that absolute model ages derived in Mare Serenitatis at a wrinkle ridge that transitions into a lobate scarp in the adjacent highlands indicate a common recent origin or reactivation (Clark et al. 2017b). In summary, previous and new results together indicate wrinkle ridge formation has occurred for more than 3.5 Gyr, perhaps nearly as early as the emplacement of the oldest mare basalts at >4 Ga (e.g., Taylor et al. 1983; Dasch et al. 1987), with most ridges having formed at ~3 Ga. However, modest activity on these structures has likely continued until up ~100 Ma, and some wrinkle ridges may have been active even more recently (see Nypaver and Thomson 2022).

6. IMPLICATIONS OF TECTONIC STRUCTURES FOR GLOBAL AND REGIONAL EVOLUTION MODELS

Models for the origin of tectonic stress on the Moon are closely tied to the two scales of the observed deformation, regional and global. Regional-scale stresses are clearly expressed in the mare basins by near side mare wrinkle ridges and basin-related graben. Most of the tectonism associated with the mare took place between ~3.5 and 2.4 Ga (e.g., Yue et al. 2017), but some tectonic activity has continued until much more recently (e.g., Williams et al. 2016; Clark et al. 2017a), as evidenced in particular by younger wrinkle ridges (Section 5.2.2). In addition, the presence of concentric extensional structures around some mare basins (Fig. 8) is likely indicative of regional basin-related stresses. Lastly, some extensional structures have been proposed to be underlain by dikes (see Section 4.3.3) (e.g., Head and Wilson 1993; Klimczak 2014), which would have formed as a consequence of dilational stresses (e.g., Pollard et al. 1983).

Global-scale stresses are evidenced by the widespread occurrence of ancient buried dikes (see Section 4.5) (Andrews-Hanna et al. 2013, 2014; Sawada et al. 2016) and the distribution of lobate scarps, now known to occur globally (see Section 4.1.2) (Watters et al. 2015a), with some scarps having very young ages (see Section 5.2.1) (e.g., Kumar et al. 2016; Clark et al. 2017a; van der Bogert et al. 2018). Taken together, the results above are consistent with an early global extensional stress state, followed by an extended period (likely 3.5 Ga to the present) of contractional stresses (see Section 5). Past and present-day stresses have likely also included contributions from the recession of the Moon away from the Earth, as well as diurnal solid-body tides (Watters et al. 2019; Matsuyama et al. 2021).

6.1. Models for regional tectonic stresses

The most successful class of stress models to account for spatial distribution and the relative timing of formation of the mare ridges and graben is the mascon tectonic model (Phillips et al. 1972; Melosh 1978; Solomon and Head 1979, 1980; Freed et al. 2001). The classic mascon tectonic model involves subsidence of relatively dense mare basalts inducing flexure of an impact-thinned and weakened lithosphere and resulting in basin interior radial thrust faults, a zone of strike-slip faulting, and concentric normal faulting near the basin margins (Melosh 1978; Freed et al. 2001). The lack of evidence of strike-slip faults has been addressed in several studies that have examined conditions that can affect whether strike-slip faulting is expected and if it occurs, what the spatial extent would be. First, Golombek (1985) found that the presence of a 1–3 km thick megaregolith layer would result in low near-surface stresses, and that furthermore the stresses in the underlying, higher-stiffness lithosphere would predict strike-slip faulting in a much narrower region. More generally, incorporation of a realistic failure criterion (Freed et al. 2001) was also found to predict a smaller region of faulting (cf. the region where strike-slip stresses are predicted). Second, the stress evolution, which depends on both the time-dependent loading history and the rheology as seen in models for volcano growth on Mars (McGovern and Solomon 1993; Schultz and Zuber 1994) and lunar basins (Schultz and Zuber 1994; Freed et al. 2001), can affect the extent of strike-slip faulting (Freed et al. 2001). Furthermore, the use of a faulting style criterion that accounts for transitional faulting and considerations of planetary curvature can also minimize the extent of strike-slip faulting (Freed et al. 2001). Finally, the dominance of concentric rather than radial wrinkle ridges can also be explained by an initially super-isostatic basin model, and a uniform thickness of mare basalt fill (Freed et al. 2001; Wieczorek et al. 2006).

GRAIL data have also revealed the presence of ancient tectonic features, specifically linear Bouguer gravity gradient anomalies that border Procellarum, interpreted as dikes that represent an early episode of regional-scale rifting (Andrews-Hanna et al. 2014). The timing and geodynamic mechanism responsible for this early episode of rifting remains unknown. The structures clearly pre-date the overlying mare, which date to ~3.51 Ga (Hiesinger et al. 2010). Thermal contraction of the Procellarum KREEP (Potassium, Rare Earth Elements, and Phosphorus) Terrane (PKT) (Jolliff et al. 2000; Wieczorek and Phillips 2000; Grimm 2013) contained within the pattern of structures provides a simple mechanism for explaining the inferred extensional tectonics (Andrews-Hanna et al. 2014). The high concentration of heat producing elements in the crust and upper mantle in this region would have led to warmer temperatures, as well as a faster rate of cooling over time than experienced by the surrounding feldspathic highlands terrane. As the crust within the PKT cooled and contracted, extension is predicted around its periphery, consistent with the inferred rifting. However, it is also possible that this rifting reflects a more dynamic mechanism related to the patterns of mantle convection associated with this region (Laneuville et al. 2013).

The Procellarum border structures have also clearly influenced later tectonics in the region. Associated with these gravity anomalies are sets of parallel wrinkle ridges in the overlying maria. These wrinkle ridges occur outside mascon basins, in particular in Procellarum and Frigoris, and thus cannot be accounted for by the mascon tectonic model. They were previously identified as marking the rim of an ancient Procellarum impact basin (Whitaker 1981), though the quasi-rectangular pattern of border structures revealed by GRAIL is clearly incompatible with that interpretation. Instead, subsequent basaltic fill of the buried rifts surrounding Procellarum may have locally induced flexure, subsidence, and the formation of wrinkle ridges. An analysis of the *D*/*L* relationships of wrinkle ridges within and outside zones defined by the gradient maps in Procellarum and Frigoris, as well as those within mascons, indicates no significant difference in the distribution of maximum displacement or lengths of the measured ridges, and all populations have nearly identical values of γ (Watters 2022) (see Section 4.2.5), suggesting similar physical properties of the deformed basaltic material in these locations (see Section 4.1.4).

A comparison of the maximum relief of wrinkle ridges within and outside of mare mascons indicates there is no statistically significantly difference, suggesting comparable levels of contractional strain in non-mascon mare (Schleicher et al. 2019). Thus, the presence of a mascon may not strongly influence the amount of subsidence and contraction of the mare basalts. This might indicate the critical role lithospheric thickness plays in supporting the mare loads by either allowing or inhibiting subsidence and contraction (see Melosh 1978).

6.2. Global tectonic models

6.2.1. Early expansion. The randomly-oriented, narrow linear gravity anomalies observed in GRAIL data and the length and widths of the inferred intrusions suggest early lunar interior expansion (estimated radius increase of 0.6–4.9 km; Andrews-Hanna et al. 2013). Such expansion could arise from the early thermal equilibration of the Moon, if it formed with a shallow (200 to 400 km) magma ocean overlying a cooler interior (Solomon and Chaiken 1976; Solomon 1977). However, some models predict accretion of the Moon to have been accompanied by melting of the entire interior (Pritchard and Stevenson 2000), and more recent models of lunar formation by giant impact favor hotter material in the circum-terrestrial disk (Canup 2012; Ćuk and Stewart 2012; Salmon and Canup 2014). A hot start for the Moon would lead to global contraction throughout its history, in conflict with the tectonic evidence for early expansion and for limited contraction at later times (Solomon and Chaiken 1976; Solomon 1977). Alternatively, global expansion could have been brought about by the sinking of dense ilmenite-rich cumulates accompanied by high concentrations of heat producing elements associated with material enriched in KREEP following the crystallization of the magma ocean (Parmentier et al. 2002). This process would have sequestered high concentrations of heat producing elements deep within the lunar interior, causing global internal warming and expansion consistent with the constraints from GRAIL (Zhang et al. 2013). An even earlier stage of expansion during magma ocean crystallization is also possible (Elkins-Tanton and Bercovici 2014), though at this early stage in lunar evolution it is not clear if the crust would have been sufficiently strong for brittle failure and dike intrusion.

6.2.2. Global contraction and interior cooling. Observable evidence for global contraction is the record by lobate scarps. Key aspects of these tectonic features relevant to stress models are their (i) global distribution, (ii) generally small relief and length, (iii) non-random orientation, and (iv) ages that span <1 Ga (e.g., Binder and Gunga 1985; Watters et al. 2010) to the population of very young (<100 Ma; Kumar et al. 2016; Clark et al. 2017a; van der Bogert et al. 2018) scarps. Global contraction estimates from the lobate scarp population suggest 25–100 m of radial contraction over the past 800 Myr (Watters et al. 2010, 2015a).

Global contraction of the Moon is predicted by two classes of thermal history models. Large amounts of contraction (generally >2 km) are predicted by models that assume the early Moon was initially total molten (Binder and Lange 1977; Binder 1986; Pritchard and Stevenson 2000). This amount of radial contraction and the associated compressional thermal stresses of up to 350 MPa (Binder and Lange 1977; Binder and Gunga 1985) would be expected to result in large-scale lobate thrust fault scarps, perhaps comparable in scale to the large fault scarps found on Mercury (see Watters et al. 2015b; Watters 2021). It has been suggested that the absence of such large-scale thrust faults may be due to significant unexpressed contractional strain absorbed by a highly porous regolith and an underlying pervasively fractured zone (Binder and Gunga 1985; Pritchard and Stevenson 2000). However, these levels of compressional stress are at odds with the discovery of relatively young graben on the Moon (Watters et al. 2012; French et al. 2015). Areas of localized extension would be expected to be mostly or completely suppressed by such high late-stage compressional stresses (Watters et al. 2012).

An alternative model that limits the amount of radial contraction and circumvents the need for a total molten state involves an early Moon with an initially relatively cold, deep mantle overlain by a hot magma ocean. In this model, the total decrease in radius after 3.8 Ga is < 1 km and predicted surface horizontal thermal stresses are ~ 100 MPa or less (Solomon and Chaiken 1976; Solomon and Head 1979, 1980).

Zhang et al. (2013) examined the effects of cumulate mantle overturn (after magma ocean solidification) with an insulating megaregolith on lunar interior heat loss. They conclude that the low thermal conductivity of the regolith layer and deep heat-producing elements are necessary for early expansion and to limit contraction to < 1 km. This combination of effects, a cool interior due to mantle overturn and an insulating regolith, might eliminate the need for a cold central interior immediately post-accretion accretion invoked by Solomon (1977, 1986).

Finally, radial global contraction from continued cooling of a hot interior that includes a still liquid outer core (as required by the observations of Weber et al. 2011) is the likely dominant source of present-day stress, contributing stresses estimated to be more than 2 MPa, but less than 10 MPa (Watters et al. 2010, 2015a, 2019; Matsuyama et al. 2021). This is important for understanding the young population of lunar thrust faults.

6.2.3. Global tidal stresses and despinning. Global contraction, absent of other influences, is expected to generate horizontally isotropic compressional stresses (Watters et al. 2015a). The resulting population of thrust faults should be uniformly distributed but without preferred orientations. An analysis of the distribution of orientations of mapped lobate scarps shows there is a distinctly non-random pattern; the orientations of many scarps are broadly north–south at low to mid latitudes and east–west at high latitudes (Fig. 2; Section 4.1.2) (Watters et al. 2015a). Ancient far side basins and the near side mare basins introduce mechanical inhomogeneities that may play a role in locally orienting the stresses, but the large-scale distribution of orientations suggests that other global-scale stresses have influenced the formation of the thrust faults.

Tidal forces are an additional source of global stress acting on the Moon, both in the distant past and at present. Stresses associated with despinning and relaxation of a rotational bulge result in contraction and north–south-oriented thrust faults in the region in and around the sub-Earth and anti-Earth points and extension and east–west-oriented normal faulting in the polar regions (Melosh 1977, 1980).

Tidal despinning likely peaked early in the Moon's evolution and thus cannot account for the population of young faults scarps. Although global contraction is likely the dominant source of present day stress, two other sources of tidal stress are acting on the Moon at present: stresses from orbital recession and Earth-raised diurnal tides (Watters et al. 2015a, 2019; Matsuyama et al. 2021). The magnitude of stresses due to orbital recession is a function of the distance the satellite has receded over a period of time and the value of Love number h_2, the vertical displacement in response to a gravitational potential (Melosh 1980; Collins et al. 2010). Solid body diurnal tidal stresses are induced by the Earth as the Moon moves from perigee to apogee. Stresses from recession accumulate over time of up to ~ 20 to 40 kPa and diurnal solid body tides reach a maximum of 5 kPa (Watters et al. 2015a, 2019; Matsuyama et al. 2021). Although relatively small in magnitude, stresses from orbital recession σ_r and diurnal tides σ_t superimposed on stresses from global contraction σ_c will result in a net non-isotropic compressional stress field σ_n where $\sigma_c \gg \sigma_r > \sigma_t$. Predicted fault orientations from the combination of $\sigma_c + \sigma_r + \sigma_t$ are generally in good agreement with the observed orientations of the lobate scarps, markedly different from faults with random orientations from isotropic contraction (Fig. 12) (Watters et al. 2015a, 2019; Matsuyama et al. 2021).

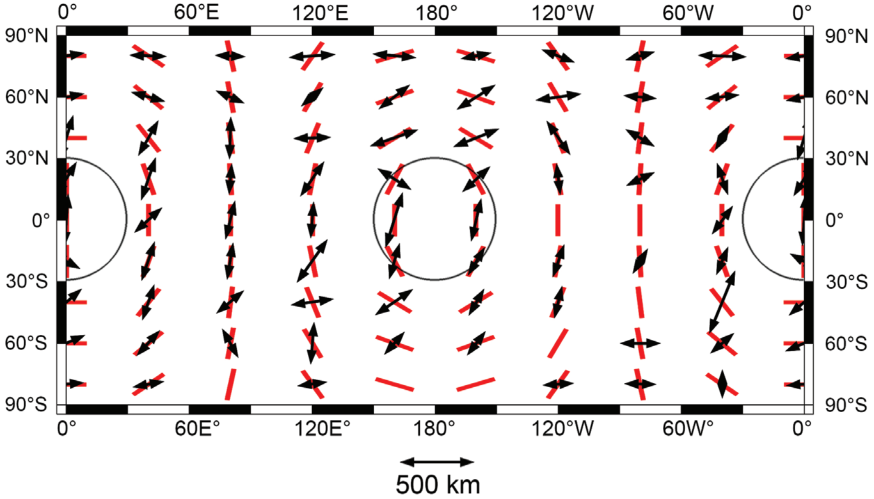

Figure 12. Plot of lobate scarp orientation vectors and orientations of predicted faults. Vectors (**black double arrows**) are the median orientations of over 3,200 lobate scarps sampled in areas with dimensions of 40° longitude by 20° latitude and scaled by total length of structures in sampled areas. **Thin black full and half circles** represent the anti-Earth and sub-Earth zones, respectively. Predicted fault trajectories (**red lines**) represent the orientation orthogonal to the most compressive stress due to the combination of global contraction, recession stresses, and diurnal tidal stresses at apogee (after Watters et al. 2015b).

6.2.4. True polar wander. Recent analysis of orbiting neutron spectrometer data indicates that polar hydrogen deposits do not match the expected distribution of water ice inferred from present-day lunar temperatures (Siegler et al. 2016). The observed distribution of remnant polar hydrogen is consistent with true polar wander (Siegler et al. 2016). The change in the spin axis occurs when a body reorients itself relative to its axis of rotation driven by mass redistribution (Matsuyama and Nimmo 2008) with the reorientation direction roughly perpendicular to the tidal axis (Melosh 1980; Collins et al. 2010). Siegler et al. (2016) attribute the change in the Moon's moments of inertia due to a low-density thermal anomaly beneath Procellarum, related to the radiogenic-rich PKT. True polar wander contributes an additional component of stress to the current lunar stress state (Collins et al. 2010; Watters et al. 2019; Matsuyama et al. 2021). Stresses from ~3° of true polar wander over the last 1 billion years are estimated to contribute up to 8 kPa (Watters et al. 2019). These stresses induce extension in the region leading the reorientation direction because the spin axis there must lengthen, and contraction is induced in the trailing region because the spin axis there must shorten (Leith and McKinnon 1996; Matsuyama and Nimmo 2008; Collins et al. 2010). Although not large compared to stresses due to global contraction, stresses from true polar wander are comparable in magnitude to diurnal tidal stresses (Watters et al. 2015a, 2019; Matsuyama et al. 2021). A relatively low level of compressional stress in the lunar lithosphere is supported by the presence of a population of relatively young small-scale graben (Watters et al. 2012; French et al. 2015). For these small graben to form, extensional stresses must locally exceed the background compressional stresses, and thus the magnitude of the compressional stresses cannot be large (Watters et al. 2012).

7. CONCLUSIONS AND OUTSTANDING QUESTIONS

Recent high-resolution imagery, topography, and gravity datasets have led to substantial advances in our understanding of lunar tectonism and its implications for the evolution of stresses in the lunar lithosphere. The ancient tectonic structures revealed by GRAIL reflect an early period of lunar tectonics that was more dynamic than its later history. Unlike the majority of later tectonics, the earliest tectonism was dominantly extensional, including both the ancient, randomly-oriented intrusions associated with early global expansion (Andrews-Hanna et al. 2013) and the Procellarum border structures associated with rifting at the margins of the PKT (Andrews-Hanna et al. 2014). The ancient lunar surface may have been crossed by numerous large-scale rift zones, graben swarms, or collapse pits, which were later destroyed by impacts and buried beneath the maria.

Subsequent near side tectonics reflects the combined effects of global interior thermal evolution and regional stresses associated with the mare-filled basins. From a global perspective, the evolution of crustal stresses on the Moon, like other single-plate rocky bodies in our solar system, likely progressed from an early phase of dominantly extensional stresses due to bulk interior heating to a later stage dominated by compressional stress due to bulk interior cooling. High-resolution mapping of lobate scarps has revealed these to be the most ubiquitous among the various types of lunar structures and has confirmed them to be globally distributed, solidifying the case (e.g., Binder 1982; Watters and Johnson 2010) that they are the surface manifestation of interior cooling and contraction. Their small reliefs indicate that contraction has been limited in comparison with that of Mercury (e.g., Watters and Nimmo 2010; Byrne et al. 2014; Watters et al. 2015b; Watters 2021), as expected on the basis of the small lunar core (Weber et al. 2011). Estimates of crustal shortening from lobate scarp reliefs suggest between 25 m and 100 m of radial contraction over the past ~800 Myr (Watters et al. 2010, 2015a), placing quantitative new constraints on thermal evolution models. The N–S orientations of these features at low-to-mid latitudes and E–W orientations at higher latitudes are incompatible with the random orientations predicted by contraction of a mechanically isotropic lithosphere and indicate that additional long-wavelength stresses play a role in the locations and/or orientations of lobate scarp formation. Tidal stresses, in combination with thermal contraction stresses, successfully predict lobate scarp orientations (Watters et al. 2015a, 2019; Matsuyama et al. 2021). The very young population of lobate scarps (Watters et al. 2010, 2012, 2015a; van der Bogert et al. 2018) suggests that global contraction has been continuing until very recently. Furthermore, re-analysis of the locations of shallow moonquakes indicates that several have occurred within 30 km of a mapped lobate scarp (Watters et al. 2019), and in combination with other evidence for recent ground motions on the lunar surface, provides the tantalizing suggestion of ongoing tectonism today (Watters et al. 2019). The new discovery of small-scale, young graben in association with contractional features indicates that at least locally recent (or even present-day) extensional stresses can overcome compressional stresses.

New data sets for wrinkle ridges (Yue et al. 2015; Thompson et al. 2017) and graben (Nahm et al. 2018) are consistent with the majority of these structures being basin-localized, resulting from loading by mare basalts that flooded the impact basins and associated topographically low elevations introduced localized stresses across much of near side. Wrinkle ridges around the periphery of Procellarum and Frigoris may have been influenced by similar volcanic loading in association with lavas-filled rifts and underlying dikes (Andrews-Hanna et al. 2014). However, is there a greater influence on wrinkle ridge formation in these non-mascon mare units?

The wealth of new data from recent lunar missions is exposing some of the gaps in the current understanding of tectonic processes on the Moon. One emerging question is the role mascons play in the tectonic deformation of the mare basalts. Wrinkle ridges are present in both mascon and non-mascon mare, yet a study by Schleicher et al. (2019) finds no significant evidence of ridges with greater relief, suggesting comparable levels of contractional strain. This may be an indication of the critical role lithospheric thickness and/or strength has in controlling subsidence and contraction of mare sequences.

Additionally, there remains an outstanding question involving lunar tectonics that directly relates to models for the origin of the Moon. What insight does very recent tectonic activity provide about the initial thermal state of a newly accreted Moon? Compressional stress levels and amounts of post late heavy bombardment radial contraction predicted by some thermal history models that invoke an initial totally molten Moon are incompatible with the magnitude of stresses inferred from the population of young lobate thrust fault scarps. Can the combination of a cool interior from cumulate mantle overturn after solidification of a magma ocean and an insulating megaregolith limit global contraction of an initial total molten Moon (as suggested by Zhang et al. 2013), or are there other early conditions or effects that contributed? Perhaps the most intriguing question is whether the Moon is still tectonically active. The possible link between multiple lobate scarps and recorded shallow moonquakes supports a tectonically active Moon (Watters et al. 2019). Does a still hot lunar interior that includes a liquid outer core, required by the observations of Weber et al. (2011), make current radial global contraction and tectonic activity inevitable?

ACKNOWLEDGMENTS

We wish to thank Walter Kiefer, Pat McGovern, and an anonymous reviewer for their helpful, careful and insightful comments and suggestions that greatly improved the chapter, and Clive Neal for a careful read and final edits. ALN funded by Alexander von Humboldt Stiftung/Foundation Postdoctoral Fellowship at DLR. CLJ acknowledges support from the Natural Sciences and Engineering Research Council of Canada. This work was supported by the LRO Project, and an ASU LROC Contract to TRW.

REFERENCES

Allemand P, Thomas PG (1995) Localization of Martian ridges by impact craters: Mechanical and chronological implications. J Geophys Res Planets 100:3251–3262

Anderson KA, Lin RP, McCoy JE, McGuire RE, Russell CT, Coleman PJ (1976) The large magnetized region associated with Rima Sirsalis. Lunar and Planetary Institute, Houston, Abstract #1006

Anderson KA, Lin RP, McGuire RE, McCoy JE, Russell CT, Coleman Jr PJ (1977) Linear magnetization feature associated with Rima Sirsalis. Earth Planet Sci Lett 34:141–151

Andrews-Hanna JC, Asmar SW, Head JW, Kiefer WS, Konopliv AS, Lemoine FG, Matsuyama I, Mazarico E, McGovern PJ, Melosh HJ (2013) Ancient igneous intrusions and early expansion of the Moon revealed by GRAIL gravity gradiometry. Science 339:675–678

Andrews-Hanna JC, Besserer J, Head JW, Howett CJA, Kiefer WS, Lucey PJ, McGovern PJ, Melosh HJ, Neumann GA, Phillips RJ (2014) Structure and evolution of the lunar Procellarum region as revealed by GRAIL gravity data. Nature 514:68

Andrews-Hanna JC, Weber RC, Garrick-Bethell I, Evans AJ, Kiefer WS, Grimm RE, Keane JT, Laneuville M, Ishihara Y, Kamata S, Matsuyama I (2023) The structure and evolution of the lunar interior. Rev Mineral Geochem 89:243–292

Arvidson R, Drozd RJ, Hohenberg CM, Morgan CJ, Poupeau G (1975) Horizontal transport of the regolith, modification of features and erosion rates on the lunar surface. Earth Moon Planets 13:67–79

Baldwin RB (1963) The Measure of the Moon. University of Chicago Press, Chicago

Baldwin RB (1965) A Fundamental Survey of the Moon. McGraw-Hill, New York

Banks ME, Watters TR, Williams NR (2017) Displacement–length relationship of thrust faults associated with lunar lobate scarps: comparison with lobate scarps on other bodies. Lunar and Planetary Institute, Houston, Abstract #2964

Banks ME, Watters TR, Robinson MS, Tornabene LL, Tran T, Ojha L, Williams NR (2012) Morphometric analysis of small-scale lobate scarps on the Moon using data from the Lunar Reconnaissance Orbiter. J Geophys Res Planets 117:E00H11

Besserer J, Nimmo F, Wieczorek MA, Weber RC, Kiefer WS, McGovern PJ, Andrews-Hanna JC, Smith DE, Zuber MT (2014) GRAIL gravity constraints on the vertical and lateral density structure of the lunar crust. Geophys Res Lett 41:5771–5777

Binder AB (1982) Post-Imbrian global lunar tectonism: Evidence for an initially totally molten Moon. Earth Moon Planets 26:117–133

Binder AB (1986) The initial thermal state of the Moon. *In:* Origin of the Moon. Hartmann WK et al. (eds) Houston, Texas, Lunar and Planetary Institute, p 425–433

Binder AB, Gunga H-C (1985) Young thrust-fault scarps in the highlands: Evidence for an initially totally molten Moon. Icarus 63:421–441

Binder AB, Lange M (1977) On the thermal history of a moon of fission origin. Earth Moon Planets 17:29–45

Boyce JM (1976) Ages of flow units in the lunar near side maria based on Lunar Orbiter IV photographs. Proc Lunar Planet Sci Conf 7:2717–2728

Bryan WB (1973) Wrinkle-ridges as deformed surface crust on ponded mare lava. Proc Lunar Planet Sci Conf 4:93–106

Byrne PK, Klimczak C, Şengör AMC, Solomon SC, Watters TR, Hauck SA (2014) Mercury's global contraction much greater than earlier estimates. Nat Geosci 7:301

Byrne PK, Klimczak C, McGovern PJ, Mazarico E, James PB, Neumann GA, Zuber MT, Solomon SC (2015) Deep-seated thrust faults bound the Mare Crisium lunar mascon. Earth Planet Sci Lett 427:183–190

Canup RM (2012) Forming a Moon with an Earth-like composition via a giant impact. Science:1226073

Casella CJ (1976) Evolution of the lunar fracture network. GSA Bull 87:226–234

Chabot NL, Hoppa GV, Strom RG (2000) Analysis of lunar lineaments: Far side and polar mapping. Icarus 147:301–308

Clark JD, Hurtado JM, Hiesinger H, van der Bogert CH, Bernhardt H (2017a) Investigation of newly discovered lobate scarps: Implications for the tectonic and thermal evolution of the Moon. Icarus 298:78–88

Clark JD, van der Bogert CH, Hiesinger H, Bernhardt H (2017b) Wrinkle ridge–lobate scarp transition of West Serenitatis: Indications for recent tectonic activity. Lunar and Planetary Institute, Houston, Abstract #1001

Collins GC, McKinnon WB, Moore JM, Nimmo F, Pappalardo RT, Prockter LM, Schenk PM (2010) Tectonics of the outer planet satellites. Planet Tectonics 11:264

Colton GW, Howard KA, Moore HJ (1972) Mare ridges and arches in Southern Oceanus Procellarum, photogeology, Apollo 16 preliminary science report, NASA Spec Publ SP-315:29–90—29–93

Coombs CR, Hawke BR, Robinson MS (1992) Pyroclastic deposits on the northwestern limb of the Moon. Lunar and Planetary Institute, Houston, Abstract #1124

Cowie PA, Scholz CH (1992a) Displacement–length scaling relationship for faults: data synthesis and discussion. J Struct Geol 14:1149–1156

Cowie PA, Scholz CH (1992b) Physical explanation for the displacement–length relationship of faults using a post-yield fracture mechanics model. J Struct Geol 14:1133–1148

Ćuk M, Stewart ST (2012) Making the Moon from a fast-spinning Earth: a giant impact followed by resonant despinning. Science 338:1047–1052

Dasch EJ, Shih C-Y, Bansal BM, Wiesmann H, Nyquist LE (1987) Isotopic analysis of basaltic fragments from lunar breccia 14321: Chronology and petrogenesis of pre-Imbium mare volcanism. Geochim Cosmochim Acta 51:3241–3254

Duennebier F, Sutton GH (1974) Thermal moonquakes. J Geophys Res 79:4351–4363

Elkins-Tanton LT, Bercovici D (2014) Contraction or expansion of the Moon's crust during magma ocean freezing? Phil Trans R Soc A 372:20130240

Ernst RE, Grosfils EB, Mège D (2001) Giant dike swarms: Earth, Venus, and Mars. Annu Rev Earth Planet Sci 29:489–534

Ferrill DA, Morris AP (2003) Dilational normal faults. J Struct Geol 25:183–196

Ferrill DA, Wyrick DY, Morris AP, Sims DW, Franklin NM (2004) Dilational fault slip and pit chain formation on Mars. GsA Today 14:4–12

Ferrill DA, Wyrick DY, Smart KJ (2011) Coseismic, dilational-fault and extension-fracture related pit chain formation in Iceland: Analog for pit chains on Mars. Lithosphere 3:133–142

Fielder G (1961) Structure of the Moon's Surface. Pergamon, London, UK

Fielder G (1963) Lunar tectonics. Q J Geol Soc 119:65–93

Freed AM, Melosh HJ, Solomon SC (2001) Tectonics of mascon loading: Resolution of the strike-slip faulting paradox. J Geophys Res Planets 106:20603–20620

French RA, Bina CR, Robinson MS, Watters TR (2015) Small-scale lunar graben: Distribution, dimensions, and formation processes. Icarus 252:95–106

French RA, Watters TR, Robinson RS (2019) Provenance of block fields along lunar wrinkle ridges. J Geophys Res 124:2970–2982

Frohlich C, Nakamura Y (2009) The physical mechanisms of deep moonquakes and intermediate-depth earthquakes: How similar and how different? Phys Earth Planet Sci 173:365–374

Gaddis LR, Staid MI, Tyburczy JA, Hawke BR, Petro NE (2003) Compositional analyses of lunar pyroclastic deposits. Icarus 161:262–280

Gaddis LR, Joy KH, Bussey BJ, Carpenter JD, Crawford IA, Elphic RC, Halekas JS, Lawrence SJ, Xiao L (2023) Recent exploration of the Moon: Science from lunar missions since 2006. Rev Mineral Geochem 89:1–51

Gilbert GK (1893) The Moon's face: a study of the origin of its features. Bull Philos Soc Washington, Bull XII

Golombek MP (1979) Structural analysis of lunar grabens and the shallow crustal structure of the Moon. J Geophys Res Solid Earth 84:4657–4666

Golombek MP (1985) Fault type predictions from stress distributions on planetary surfaces—Importance of fault initiation depth. J Geophys Res 90:3065–3074

Golombek MP, McGill GE (1983) Grabens, basin tectonics, and the maximum total expansion of the Moon. J Geophys Res Solid Earth 88:3563–3578

Golombek MP, Plescia JB, Franklin BJ (1991) Faulting and folding in the formation of planetary wrinkle ridges. Proc Lunar Planet Sci Conf 21:679–693

Golombek MP, Anderson FS, Zuber MT (2001) Martian wrinkle ridge topography: Evidence for subsurface faults from MOLA. J Geophys Res Planets 106:23811–23821

Grant JV, Kattenhorn SA (2004) Evolution of vertical faults at an extensional plate boundary, southwest Iceland. J Struct Geol 26:537–557

Grimm RE (2013) Geophysical constraints on the lunar Procellarum KREEP Terrane. J Geophys Res Planets 118:768–778

Hartmann WK, Wood CA (1971) Moon: Origin and evolution of multi-ring basins. Earth Moon Planets 3:3–78

Hauber E, Grott M, Kronberg P (2010) Martian rifts: Structural geology and geophysics. Earth Planet Sci Lett 294:393–410

Hauck SA, Dombard AJ, Phillips RJ, Solomon SC (2004) Internal and tectonic evolution of Mercury. Earth Planet Sci Lett 222:713–728

Head JW, Wilson L (1979) Alphonsus-type dark-halo craters: Morphology, morphometry, and eruption conditions. Lunar and Planetary Institute, Houston, Abstract #1186

Head JW, Wilson L (1993) Lunar graben formation due to near-surface deformation accompanying dike emplacement. Planet Space Sci 41:719–727

Head JW, Murchie SL, Prockter LM, Solomon SC, Strom RG, Chapman CR, Watters TR, Blewett DT, Gillis-Davis JJ, Fassett CI (2009) Evidence for intrusive activity on Mercury from the first MESSENGER flyby. Earth Planet Sci Lett 285:251–262

Hiesinger H, Head JW, Wolf U, Jaumann R, Neukum G (2003) Ages and stratigraphy of mare basalts in oceanus procellarum, mare nubium, mare cognitum, and mare insularum. J Geophys Res Planets 108(E7):5065

Hiesinger H, Head JW, Wolf U, Jaumann R, Neukum G (2010) Ages and stratigraphy of lunar mare basalts in Mare Frigoris and other near side maria based on crater size-frequency distribution measurements. J Geophys Res Planets 115:E03003

Hodges CA (1973) Mare ridges and lava lakes. Apollo 17 Preliminary Science Report, NASA Spec Publ SP330: 3112–3121

Howard KA, Muehlberger WR (1973) Lunar thrust faults in the Taurus-Littrow region. Apollo 17 Preliminary Science Report, NASA Spec Publ SP330:3132–3125

Jansen JC, Andrews-Hanna JC, Li Y, Lucey PG, Taylor GJ, Goossens S, Lemoine FG, Mazarico E, Head JW, Milbury C (2017) Small-scale density variations in the lunar crust revealed by GRAIL. Icarus 291:107–123

Johnson AM (1980) Folding and faulting of strain-hardening sedimentary rocks. Tectonophysics 62:251–278

Jolliff BL, Gillis JJ, Haskin LA, Korotev RL, Wieczorek MA (2000) Major lunar crustal terranes: Surface expressions and crust–mantle origins. J Geophys Res Planets 105:4197–4216

Jozwiak LM, Head JW, Zuber MT, Smith DE, Neumann GA (2012) Lunar floor-fractured craters: Classification, distribution, origin and implications for magmatism and shallow crustal structure. J Geophys Res Planets 117:E11005

Kawamura T, Lognonné P, Nishikawa Y, Tanaka S (2017) Evaluation of deep moonquake source parameters: Implication for fault characteristics and thermal state. J Geophys Res Planets 122:1487–1504

Keane JT, Matsuyama I (2014) Evidence for lunar true polar wander and a past low-eccentricity, synchronous lunar orbit. Geophys Res Lett 41:6610–6619

Kiefer WS, Swafford LC (2006) Topographic analysis of Devana Chasma, Venus: Implications for rift system segmentation and propagation. J Struct Geol 28:2144–2155

Klimczak C (2014) Geomorphology of lunar grabens requires igneous dikes at depth. Geology 42:963–966

Konopliv AS, Park RS, Yuan DN, Asmar SW, Watkins MM, Williams JG, Fahnestock E, Kruizinga G, Paik M, Strekalov D (2014) High-resolution lunar gravity fields from the GRAIL Primary and extended missions. Geophys Res Lett 41:1452–1458

Krassilnikov AS, Head JW (2003) Novae on Venus: Geology, classification, and evolution. J Geophys Res Planets 108(E9):5108

Kumar PS, Sruthi U, Krishna N, Lakshmi KJP, Menon R, Amitabh, Krishna BP, Kring DA, Head JW, Goswami JN, Kumar ASK (2016) Recent shallow moonquake and impact-triggered boulder falls on the Moon: New insights from the Schrödinger basin. J. Geophys Res Planets 121:147–179

Kumar PS, Mohanty R, Lakshmi KJP, Raghukanth STG, Dabhu AC, Rajasekhar RP, Menon R (2019) The seismically active lobate scarps and coseismic lunar boulderavalanches triggered by 3 January 1975 (MW 4.1) shallow moonquake. Geophys Res Lett 46:7972–7981

Laneuville M, Wieczorek MA, Breuer D, Tosi N (2013) Asymmetric thermal evolution of the Moon. J Geophys Res Planets 18:1435–1452

Leith AC, McKinnon WB (1996) Is there evidence for polar wander on Europa? Icarus 120:387–398

Lemoine FG, Goossens S, Sabaka TJ, Nicholas JB, Mazarico E, Rowlands DD, Loomis BD, Chinn DS, Neumann GA, Smith DE (2014) GRGM900C: A degree 900 lunar gravity model from GRAIL primary and extended mission data. Geophys Res Lett 41:3382–3389

Li B, Ling Z, Zhanga J, Chen J, Ni Y, Liu C (2018) Displacement–length ratios and contractional strains of lunar wrinkle ridges in Mare Serenitatis and Mare Tranquillitatis. J Structural Geol 109:27–37

Lucchitta BK (1976) Mare ridges and related highland scarps-Result of vertical tectonism. Geochim Cosmochim Acta 3 (Suppl): 2761–2782

Lucchitta BK (1977) Topography, structure, and mare ridges in southern Mare Imbrium and northern Oceanus Procellarum. Proc Lunar Science Conf 8, Geochim Cosmochim Acta **3** (Suppl.): 26912703

Lucchitta BK, Watkins JA (1978) Age of graben systems on the Moon. Proc Lunar Planet Sci Conf 9. Geochim Cosmochim Acta 3 (Suppl): 3459–3472

Mangold N, Allemand P, Thomas PG (1998) Wrinkle ridges of Mars: Structural analysis and evidence for shallow deformation controlled by ice-rich décollements. Planet Space Sci 46:345–356

Martin ES, Watters TR (2021) Topography of near side mare graben: Implications for dike-induced or passive extension formation. Icarus 354:114039

Martin ES, Watters TR (2022) Displacement–length scaling relations of near side graben: Evidence of restricted normal faults on the Moon. Icarus 388:115215

Martin ES, Kattenhorn SA, Collins GC, Michaud RL, Pappalardo RT, Wyrick DY (2017) Pit chains on Enceladus signal the recent tectonic dissection of the ancient cratered terrains. Icarus 294:209–217

Mastin LG, Pollard DD (1988) Surface deformation and shallow dike intrusion processes at Inyo Craters, Long Valley, California. J Geophys Res Solid Earth 93:13221–13235

Masursky H, Colton GW, El-Baz F, Doyle FJ (1978) Apollo over the Moon: a View from Orbit. NASA Spec Publ 362

Matsuyama I, Nimmo F (2008) Tectonic patterns on reoriented and despun planetary bodies. Icarus 195:459–473

Matsuyama, I, Kean JT, Trinh A, Beuthe, M, Watters TR (2021) Global tectonic patterns of the Moon. Icarus 358:114202

Mattingly TK, El-Baz F, Laidley RA (1972) Observations and impressions from lunar orbit. Apollo 16 Prelim Sci Rep 28-1–28-16

Maxwell TA, Phillips RJ (1978) Stratigraphic correlation of the radar-detected subsurface interface in Mare Crisium. Geophys Res Lett 5:811–814

Maxwell TA, El-Baz F, Ward SH (1975) Distribution, morphology, and origin of ridges and arches in Mare Serenitatis. Geol Soc Am Bull 86:1273–1278

McGill GE (1971) Attitude of fractures bounding straight and arcuate lunar rilles. Icarus 14:53–58

McGill GE, Schultz RA, Moore JM (2000) Fault growth by segment linkage: an explanation for scatter in maximum displacement and trace length data from the Canyonlands grabens of SE Utah: Discussion. J Struct Geol 22:135–140

McGovern PJ, Solomon SC (1993) State of stress, faulting, and eruption characteristics of large volcanoes on Mars**.** J Geophys Res 98:23553–23579

Mège D, Cook AC, Garel E, Lagabrielle Y, Cormier MH (2003) Volcanic rifting at Martian grabens. J Geophys Res Planets 108(E5):5044

Melosh HJ (1977) Global tectonics of a despun planet. Icarus 31:221–243

Melosh HJ (1978) The tectonics of mascon loading. Proc Lunar Planet Sci Conf 9:3513–3525

Melosh HJ (1980) Tectonic patterns on a reoriented planet: Mars. Icarus 44:745–751

Melosh HJ, McKinnon WB (1988) The tectonics of Mercury. *In:* Mercury. Vilas F, Chapman CR, Matthews MS (eds) University of Arizona Press, Tucson, p 374–400

Michaud RL, Pappalardo RT, Collins GC (2008) Pit chains on Enceladus: A discussion of their origin. Lunar and Planetary Institute, Houston, Abstract #1678

Montési LGJ, Zuber MT (2003a) Spacing of faults at the scale of the lithosphere and localization instability: 1. Theory. J Geophys Res Solid Earth 108(B2):21010

Montési LGJ, Zuber MT (2003b) Clues to the lithospheric structure of Mars from wrinkle ridge sets and localization instability. J Geophys Res Planets 108(E6):5048

Muehlberger WR (1974) Structural history of southeastern Mare Serenitatis and adjacent highlands. Proc Lunar Sci Conf 5, Geochim et Cosmochim Acta 1(Suppl.):101–110

Mueller K, Golombek MP (2004) Compressional structures on Mars. Annu Rev Earth Planet Sci 32:435–464

Nahm AL, Dudde A-K, Hauber E (2016) Relative ages of graben and wrinkle ridges on the near side of the Moon reveal contradictory relationships. Lunar and Planetary Institute, Houston, Abstract #1855

Nahm AL, Johnson MB, Hauber E, Watters TR, Martin ES (2018) New global map and classification of large-scale extensional structures on the Moon. Lunar and Planetary Institute, Houston, Abstract #2074

Nakamura Y (1977) HFT events: Shallow moonquakes? Phys Earth Planet Sci 14:217–223

Nakamura Y (1980) Shallow moonquakes—How they compare with earthquakes. Proc Lunar Planet Sci Conf 11:1847–1853

Nakamura Y (2005) Farside deep moonquakes and deep interior of the Moon. J Geophys Res Planets 110:E01001

Nakamura Y, Latham GV, Dorman HJ, Ibrahim A-BK, Koyama J, Horvath P (1979) Shallow moonquakes—Depth, distribution and implications as to the present state of the lunar interior. Proc Lunar Sci Conf 10:2299–2309

Nakamura Y, Latham GV, Dorman J, Harris J (1981) Passive seismic experiment long-period event catalog. Galveston Geophysics Laboratory Contribution 491:314

Nelson DM, Koeber SD, Daud K, Robinson MS, Watters TR, Banks ME, Williams NR (2014) Mapping lunar maria extents and lobate scarps using LROC image products. Lunar and Planetary Institute, Houston, Abstract #2861

Nimmo F (2004) Dynamics of rifting and modes of extension on icy satellites. J Geophys Res Planets 109:E01003

Niño F, Philip H, Chéry J (1998) The role of bed-parallel slip in the formation of blind thrust faults. J Struct Geol 20:503–516

Nypaver C, Thomson BJ (2022) New observations of recently active wrinkle ridges in the lunar mare: Implications for the timing and origin of lunar tectonics. Geophys Res Lett 49:e2022GL098975

Ono T, Kumamoto A, Nakagawa H, Yamaguchi Y, Oshigami S, Yamaji A, Kobayashi T, Kasahara Y, Oya H (2009) Lunar radar sounder observations of subsurface layers under the near side maria of the Moon. Science 323:909–912

Parmentier EM, Zhong S, Zuber MT (2002) Gravitational differentiation due to initial chemical stratification: Origin of lunar asymmetry by the creep of dense KREEP? Earth Planet Sci Lett 201:473–480

Peeples WJ, Sill WR, May TW, Ward SH, Phillips RJ, Jordan RL, Abbott EA, Killpack TJ (1978) Orbital radar evidence for lunar subsurface layering in Maria Serenitatis and Crisium. J Geophys Res Solid Earth 83:3459–3468

Phillips RJ, Conel JE, Abbott EA, Sjogren WL, Morton JB (1972) Mascons: Progress toward a unique solution for mass distribution. J Geophys Res 77:7106–7114

Phillips RJ, Adams GF, Brown Jr WE, Eggleton RE, Jackson P, Jordan RL, Peeples WJ, Porcello LJ, Ryu J, Schaber GG (1973) The Apollo 17 lunar sounder. Proc Lunar Science Conf 4, Geochim Cosmochim Acta 3(Suppl. 4): 2821–2831

Plescia JB, Golombek MP (1986) Origin of planetary wrinkle ridges based on the study of terrestrial analogs. Geol Soc Am Bull 97:1289–1299

Pollard DD, Holzhausen G (1979) On the mechanical interaction between a fluid-filled fracture and the Earth's surface. Tectonophysics 53:27–57

Pollard DD, Delaney PT, Duffield WA, Endo ET, Okamura AT (1983) Surface deformation in volcanic rift zones. Tectonophysics 94:541–584

Pritchard ME, Stevenson DJ (2000) Thermal aspects of a lunar origin by giant impact. Origin of the Earth and Moon 1:179–196

Qin C, Muirhead AC, Zhong S (2012) Correlation of deep moonquakes and mare basalts: Implications for lunar mantle structure and evolution. Icarus 220:100–105

Quaide W (1965) Rilles, ridges, and domes—Clues to maria history. Icarus 4:374–389

Robinson MS, Brylow SM, Tschimmel M, Humm D, Lawrence SJ, Thomas PC, Denevi BW, Bowman-Cisneros E, Zerr J, Ravine MA (2010) Lunar reconnaissance orbiter camera (LROC) instrument overview. Space Sci Rev 150:81–124

Roering JJ, Cooke ML, Pollard DD (1997) Why blind thrust faults do not propagate to the Earth's surface: Numerical modeling of coseismic deformation associated with thrust-related anticlines. J Geophys Res Solid Earth 102:11901–11912

Roggon L, Hetzel R, Hiesinger H, Clark JD, Hampel A, van der Bogert CH (2017) Length-displacement scaling of thrust faults on the Moon and the formation of uphill-facing scarps. Icarus 292:111–124

Rubin AM (1992) Dike-induced faulting and graben subsidence in volcanic rift zones. J Geophys Res Solid Earth 97:1839–1858

Rubin AM, Pollard DD (1988) Dike-induced faulting in rift zones of Iceland and Afar. Geology 16:413–417

Salmon J, Canup RM (2014) Accretion of the Moon from non-canonical discs. Phil Trans R Soc A 372:20130256

Sawada N, Morota T, Kato S, Ishihara Y, Hiramatsu Y (2016) Constraints on timing and magnitude of early global expansion of the Moon from topographic features in linear gravity anomaly areas. Geophy Res Lett 43:4865–4870

Schaber GG (1973) Lava flows in Mare Imbrium: Geologic evaluation from Apollo orbital photography. Proc Lunar Sci Conf 4:73–92

Schleicher LS, Watters TR, Martin AJ, Banks ME (2019) Wrinkle ridges on Mercury and the Moon within and outside of mascons. Icarus 331:226–237

Scholten F, Oberst J, Matz KD, Roatsch T, Wählisch M, Speyerer EJ, Robinson MS (2012) GLD100: The near-global lunar 100 m raster DTM from LROC WAC stereo image data. J Geophys Res Planets 117:E00H17

Schultz PH (1976a) Moon morphology: Interpretations based on Lunar Orbiter photography. University of Texas Press, Austin

Schultz PH (1976b) Floor-fractured lunar craters. Earth Moon Planets 15:241–273

Schultz RA (2000) Localization of bedding plane slip and backthrust faults above blind thrust faults: Keys to wrinkle ridge structure. J Geophys Res Planets 105:12035–12052

Schultz RA, Zuber MA (1994) Observations, models, and mechanisms of failure of surface rocks surrounding planetary surface loads. J Geophys Res 99:14691–14702

Schultz RA, Watters TR (2001) Forward mechanical modeling of the Amenthes Rupes thrust fault on Mars. Geophys Res Lett 28:4659–4662

Schultz RA, Okubo CH, Goudy CL, Wilkins SJ (2004) Igneous dikes on Mars revealed by Mars Orbiter Laser Altimeter topography. Geology 32:889–892

Schultz RA, Soliva R, Okubo CH, Mège D (2010a) Fault populations. *In*: Planetary Tectonics. Watters TR, Schultz RA (eds). Cambridge University Press, 457–510

Schultz RA, Hauber E, Kattenhorn SA, Okubo CH, Watters TR (2010b) Interpretation and analysis of planetary structures. J Struct Geol 32:855–875

Scott DH (1973) Small structures of the Taurus-Littrow region. Apollo 17 Preliminary Sci Report, NASA Spec Publ SP330:31-25–31-29

Sharpton VL (1992) Apollo 17: One giant step toward understanding the tectonic evolution of the Moon: Geology of the Apollo 17 landing site. LPI Tech Rep 92–09, Part 1:50–53

Sharpton VL, Head JW (1981) The origin of mare ridges: Evidence from basalt stratigraphy and substructure in Mare Serenitatis. Lunar and Planetary Institute, Houston, p 961–963

Sharpton VL, Head JW (1982) Stratigraphy and structural evolution of southern Mare Serenitatis: A reinterpretation based on Apollo Lunar Sounder Experiment data. J Geophys Res Solid Earth 87:10983–10998

Sharpton VL, Head JW (1988) Lunar mare ridges—Analysis of ridge-crater intersections and implications for the tectonic origin of mare ridges. Proc Lunar Sci Conf 18:307–317

Siegler MA, Miller RS, Keane JT, Laneuville M, Paige DA, Matsuyama I, Lawrence DJ, Crotts A, Poston MJ (2016) Lunar true polar wander inferred from polar hydrogen. Nature 531:480–484

Soliva R, Schultz RA, Benedicto A (2005) Three-dimensional displacement-length scaling and maximum dimension of normal faults in layered rocks. Geophys Res Lett 32:L16302

Solomon SC (1977) The relationship between crustal tectonics and internal evolution in the Moon and Mercury. Phys Earth Planet Sci 15:135–145

Solomon SC (1986) On the early thermal state of the Moon. *In:* Origin of the Moon. Hartmann WK, Phillips RJ, Taylor GJ (eds) Houston, Texas, Lunar and Planetary Institute, p 435–452

Solomon SC, Chaiken J (1976) Thermal expansion and thermal stress in the moon and terrestrial planets—Clues to early thermal history. Proc Lunar Sci Conf 7:3229–3243

Solomon SC, Head JW (1979) Vertical movement in mare basins: Relation to mare emplacement, basin tectonics, and lunar thermal history. J Geophys Res Solid Earth 84:1667–1682

Solomon SC, Head JW (1980) Lunar mascon basins: Lava filling, tectonics, and evolution of the lithosphere. Rev Geophys 18:107–141

Srnka LJ, Hoyt JL, Harvey JVS, McCoy JE (1979) A study of the Rima Sirsalis lunar magnetic anomaly. Phys Earth Planet Sci 20:281–290

Strom RG (1964) Analysis of lunar lineaments, I: Tectonic maps of the Moon. Commun Lunar Planet Lab 2:205–216

Strom RG (1972) Lunar mare ridges, rings and volcanic ring complexes. *In*: The Moon. Springer, p 187–215

Strom RG, Trask NJ, Guest JE (1975) Tectonism and volcanism on Mercury. J Geophys Res 80:2478–2507

Tanaka KL, Golombek MP, Banerdt WB (1991) Reconciliation of stress and structural histories of the Tharsis region of Mars. J Geophys Res Planets 96:15617–15633

Taylor LA, Shervais JW, Hunter RH, Shih C-Y, Bansal BM, Wooden J, Nyquist LE, Laul JC (1983) Pre-4.2 AQ mare-basalt volcanism in the lunar highlands. Earth Planet Sci Lett 66:33–47

Thompson TJ, Robinson MS, Watters TR, Johnson MB (2017) Global lunar wrinkle ridge identification and analysis. Lunar and Planetary Institute, Houston, Abstract #2665

Tija HD (1970) Lunar wrinkle ridges indicative of strike-slip faulting. Geol Soc Am Bull 81:3095–3100

Trask NJ (1971) Geologic comparison of mare materials in the lunar equatorial belt, including Apollo 11 and Apollo 12 landing sites. Geological Survey Research 1971, Chapter D: US Geol Survey Prof Paper 750-D:D138–D144

Valantinas A, Schultz PH (2020) The origin of neotectonics on the lunar near side. Geology 48:649–653

van der Bogert CH, Hiesinger H, Banks ME, Watters TR, Robinson MS (2012) Derivation of absolute model ages for lunar lobate scarps. Lunar and Planetary Institute, Houston, Abstract #1847

van der Bogert CH, Clark JD, Hiesinger H, Banks ME, Watters TR, Robinson MS (2018) How old are lunar lobate scarps? 1. Seismic resetting of crater size–frequency distributions. Icarus 306:225–242

Walsh JJ, Watterson J (1988) Analysis of the relationship between displacements and dimensions of faults. J Struct Geol 10:239–247

Watters TR (1988) Wrinkle ridge assemblages on the terrestrial planets. J Geophys Res Solid Earth 93:10236–10254

Watters TR (1991) Origin of periodically spaced wrinkle ridges on the Tharsis Plateau of Mars. J Geophys Res Planets 96:15599–15616

Watters TR (1992) System of tectonic features common to Earth, Mars, and Venus. Geology 20:609–612

Watters TR (1993) Compressional tectonism on Mars. J Geophys Res Planets 98:17049–17060

Watters TR (2003) Thrust faults along the dichotomy boundary in the eastern hemisphere of Mars. J Geophys Res Planets 98:17049–17060

Watters TR (2004) Elastic dislocation modeling of wrinkle ridges on Mars. Icarus 171:284–294

Watters, TR (2021) A case for limited global contraction of Mercury. Commun Earth Environ 2:9

Watters TR (2022) Lunar wrinkle ridges and the evolution of the near side lithosphere. J Geophys Res Planets 127: e2021JE007058

Watters TR, Johnson CL (2010) Lunar tectonics. *In*: Planetary Tectonics. Watters TR, Schultz RA (eds). Cambridge University Press, New York, p 121–182

Watters TR, Nimmo F (2010) The tectonics of Mercury. Planetary tectonics. *In*: Planetary Tectonics. Watters TR, Schultz RA (eds). Cambridge University Press, New York, p 15–80

Watters TR, Robinson MS (1997) Radar and photoclinometric studies of wrinkle ridges on Mars. J Geophys Res Planets 102:10889–10903

Watters TR, Schultz RA (2010) Planetary Tectonics. Cambridge University Press, New York

Watters TR, Robinson MS, Cook AC (1998) Topography of lobate scarps on Mercury: New constraints on the planet's contraction. Geology 26:991–994

Watters TR, Schultz RA, Robinson MS (2000) Displacement-length relations of thrust faults associated with lobate scarps on Mercury and Mars: Comparison with terrestrial faults. Geophys Res Lett 27:3659–3662

Watters TR, Schultz RA, Robinson MS, Cook AC (2002) The mechanical and thermal structure of Mercury's early lithosphere. Geophys Res Lett 29

Watters TR, Solomon SC, Robinson MS, Head JW, André SL, Hauck SA, Murchie SL (2009) The tectonics of Mercury: The view after MESSENGER's first flyby. Earth Planet Sci Lett 285:283–296

Watters TR, Robinson MS, Beyer RA, Banks ME, Bell JF, Pritchard ME, Hiesinger H, Van Der Bogert CH, Thomas PC, Turtle EP (2010) Evidence of recent thrust faulting on the Moon revealed by the Lunar Reconnaissance Orbiter Camera. Science 329:936–940

Watters TR, Thomas PC, Robinson MS (2011) Thrust faults and the near-surface strength of asteroid 433 Eros. Geophys Res Lett 38

Watters TR, Robinson MS, Banks ME, Tran T, Denevi BW (2012) Recent extensional tectonics on the Moon revealed by the Lunar Reconnaissance Orbiter Camera. Nat Geosci 5:181

Watters TR, Robinson MS, Collins GC, Banks ME, Daud K, Williams NR, Selvans MM (2015a) Global thrust faulting on the Moon and the influence of tidal stresses. Geology 43:851–854

Watters TR, Selvans MM, Banks ME, Hauck SA, Becker KJ, Robinson MS (2015b) Distribution of large-scale contractional tectonic landforms on Mercury: Implications for the origin of global stresses. Geophys Res Lett 42:3755–3763

Watters TR, Daud K, Banks ME, Selvans MM, Chapman CR, Ernst CM (2016) Recent tectonic activity on Mercury revealed by small thrust fault scarps. Nat Geosci 9:743–747

Watters TR, Weber RC, Collins GC, Howley IJ, Schmerr NC, Johnson CJ (2019) Shallow seismic activity and young thrust faults on the Moon. Nat Geosci 12:411–418

Weber RC, Bills BG, Johnson CL (2010) A simple physical model for deep moonquake occurrence times. Phys Earth Planet Sci 182:152–160

Weber RC, Lin P-Y, Garnero EJ, Williams Q, Lognonne P (2011) Seismic detection of the lunar core. Science 331:309–312

Weber RC, Dimech J-L, Phillips D, Molaro J, Schmerr NC (2017) A new moonquake catalog from Apollo 17 seismic data I: Lunar Seismic Profiling Experiment: Thermal moonquakes and implications for surface processes. AGU Fall Meeting:P44B-09

Whitaker EA (1966) The Surface of the Moon. Johns Hopkins Press, Baltimore

Whitaker EA (1981) The lunar Procellarum basin. *In*: Multi-ring basins: Formation and evolution. Schultz PH, Merrill RB (eds) Pergamon Press, New York, p 105–111

Wieczorek MA, Phillips RJ (2000) The "Procellarum KREEP Terrane": Implications for mare volcanism and lunar evolution. J Geophys Res Planets 105:20417–20430

Wieczorek MA, Jolliff BL, Khan A, Pritchard ME, Weiss BP, Williams JG, Hood LL, Righter K, Neal CR, Shearer CK (2006) The constitution and structure of the lunar interior. Rev Mineral Geochem 60:221–364

Wieczorek MA, Neumann GA, Nimmo F, Kiefer WS, Taylor GJ, Melosh HJ, Phillips RJ, Solomon SC, Andrews-Hanna JC, Asmar SW, Konopliv AS (2012) The crust of the Moon as seen by GRAIL. Science 339:6120

Wilhelms DE (1987) The geologic history of the Moon. Washington, D.C., U.S. Government Printing Office

Williams NR, Watters TR, Pritchard ME, Banks ME, Bell JF (2013) Fault dislocation modeled structure of lobate scarps from Lunar Reconnaissance Orbiter Camera digital terrain models. J Geophys Res Planets 118:224–233

Williams NR, Bell JF, Watters TR, Banks ME, Robinson MS (2014) Timing and controls of tectonic deformation in Mare Frigoris. Lunar and Planetary Institute, Houston, Abstract #2684

Williams NR, Bell JF, Shirzaei M, Watters TR, Banks ME, Daud K, French RA (2016) Evidence for active tectonism at the lunar surface. Lunar and Planetary Institute, Houston, Abstract #2808

Williams NR, Bell JF, Watters TR, Banks ME, Daud K, French RA (2019) Evidence for recent and ancient faulting at Mare Frigoris and implications for lunar tectonic evolution. Icarus 326:151–161

Wilson L, Head JW (1996) Lunar linear rilles as surface manifestations of dikes: theoretical considerations. Lunar and Planetary Institute, Houston, Abstract, 1445–1446

Wilson L, Head JW (2002) Tharsis-radial graben systems as the surface manifestation of plume-related dike intrusion complexes: Models and implications. J Geophys Res Planets 107, https://doi.org/10.1029/2001JE001593

Wilson L, Head JW (2018) Lunar floor-fractured craters: Modes of dike and sill emplacement and implications of gas production and intrusion cooling on surface morphology and structure. Icarus 305:105–122

Wilson L, Hawke BR, Giguere TA, Petrycki ER (2011) An igneous origin for Rima Hyginus and Hyginus crater on the Moon. Icarus 215:584–595

Wojtal SF (1996) Changes in fault displacement populations correlated to linkage between faults. J Struct Geol 18:265–279

Wu SSC, Doyle FJ (1990) Topographic mapping. *In*: Planetary Mapping. Greeley R, Batson RM (eds). Cambridge University Press, Cambridge, p 169–207

Xiao L, Zhu P, Fang G, Xiao Z, Zou Y, Zhao J, Zhao N, Yuan Y, Qiao L, Zhang X, Zhang H, Wang J, Huang J, Huang Q, He Q, Zhou B, Ji Y, Zhang Q, Shen S, Li Y, Gao Y (2015) A young multilayered terrane of the northern Mare Imbrium revealed by Chang'E-3 mission, Science 347:1226–1229

Xiao Z, Huang Q, Zeng Z, Xiao L (2017) Small graben in the southeastern ejecta blanket of the lunar Copernicus crater: Implications for recent shallow igneous intrusion on the Moon. Icarus 298:89–97

Xiao Z, Zeng Z, Xiao L, Fa W, Huang Q (2010) Origin of pit chains in the floor of lunar Copernican craters. Sci China Phys Mech Astronom 53:2145–2159

Young RA, Brennan WJ, Wolfe RW, Nichols DJ (1973) Volcanism in the Lunar maria. Apollo 17 Preliminary Science Report, NASA Spec Publ SP-330: 31-1–31-11

Yue Z, Michael GG, Di K, Liu JJ (2017) Global survey of lunar wrinkle ridge formation times. Earth Planet Sci Lett 477:14–20

Yue Z, Li W, Di K, Liu Z, Liu JJ (2015) Global mapping and analysis of lunar wrinkle ridges. J Geophys Res Planets 120:978–994

Zhang N, Parmentier EM, Liang Y (2013) Effects of lunar cumulate mantle overturn and megaregolith on the expansion and contraction history of the Moon. Geophys Res Lett 40:5019–5023

Zuber MT (1995) Wrinkle ridges, reverse faulting, and the depth penetration of lithospheric strain in Lunae Planum, Mars. Icarus 114:80–92

Zuber MT, Aist LL (1990) The shallow structure of the Martian lithosphere in the vicinity of the ridged plains. J Geophys Res Solid Earth 95:14215–14230

Zuber MT, Smith DE, Lehman DH, Hoffman TL, Asmar SW, Watkins MM (2013a) Gravity Recovery and Interior Laboratory (GRAIL): Mapping the lunar interior from crust to core. Space Sci Rev 178:3–24

Zuber MT, Smith DE, Watkins MM, Asmar SW, Konopliv AS, Lemoine FG, Melosh HJ, Neumann GA, Phillips RJ, Solomon SC (2013b) Gravity field of the Moon from the Gravity Recovery and Interior Laboratory (GRAIL) mission. Science 339:668–671